

Article

Landsat-8 Operational Land Imager Radiometric Calibration and Stability

Brian Markham ^{1,*}, Julia Barsi ², Geir Kvaran ³, Lawrence Ong ², Edward Kaita ², Stuart Biggar ⁴, Jeffrey Czapla-Myers ⁴, Nischal Mishra ⁵ and Dennis Helder ⁵

¹ Biospheric Sciences Laboratory, Code 618, NASA/GSFC, Greenbelt, MD 20771, USA

² Science Systems and Applications, Inc., Code 618, NASA/GSFC, Greenbelt, MD 20771, USA;
E-Mails: Julia.A.Barsi@nasa.gov (J.B.); Lawrence.Ong@nasa.gov (L.O.);
Edward.Kaita-1@nasa.gov (E.K.)

³ Ball Aerospace & Technologies Corp., 1600 Commerce Street, Boulder, CO 80301, USA;
E-Mail: gkvaran@ball.com

⁴ Remote Sensing Group, College of Optical Sciences, University of Arizona,
1630 E University Blvd, Tucson, AZ 85721, USA;
E-Mails: biggar@optics.arizona.edu (S.B.); jscm@optics.arizona.edu (J.C.-M.)

⁵ College of Engineering, South Dakota State University, Brookings, SD 57007, USA;
E-Mails: Nischal.Mishra@sdstate.edu (N.M.); Dennis.Helder@sdstate.edu (D.H.)

* Author to whom correspondence should be addressed; E-Mail: Brian.L.Markham@nasa.gov;
Tel.: +1-301-614-6608; Fax: +1-301-614-6695.

External Editors: James C. Storey and Prasad S. Thenkabail

Received: 30 July 2014; in revised form: 28 October 2014 / Accepted: 24 November 2014 /

Published: 9 December 2014

Abstract: The Landsat-8 Operational Land Imager (OLI) was radiometrically calibrated prior to launch in terms of spectral radiance, using an integrating sphere source traceable to National Institute of Standards and Technology (NIST) standards of spectral irradiance. It was calibrated on-orbit in terms of reflectance using diffusers characterized prior to launch using NIST traceable standards. The radiance calibration was performed with an uncertainty of ~3%; the reflectance calibration to an uncertainty of ~2%. On-orbit, multiple calibration techniques indicate that the sensor has been stable to better than 0.3% to date, with the exception of the shortest wavelength band, which has degraded about 1.0%. A transfer to orbit experiment conducted using the OLI's heliostat-illuminated diffuser suggests that some bands increased in sensitivity on transition to orbit by as much as 5%, with an uncertainty of

~2.5%. On-orbit comparisons to other instruments and vicarious calibration techniques show the radiance (without a transfer to orbit adjustment), and reflectance calibrations generally agree with other instruments and ground measurements to within the uncertainties. Calibration coefficients are provided with the data products to convert to either radiance or reflectance units.

Keywords: Landsat; radiometry; calibration

1. Introduction

Landsat-8 was launched on 11 February 2013 with two Earth imaging sensors on-board: The Operational Land Imager (OLI) that will be discussed in this paper and the Thermal Infrared Sensor (TIRS). The OLI, built and tested by Ball Aerospace & Technologies Corp ((BATC), Boulder, CO, USA), images the Earth in 9 spectral bands as described in [1]. The primary characteristics of the OLI instrument relevant to this paper are presented in Table 1. Throughout the paper the spectral bands will be referred to by their band number, name or center wavelength. It is important to note that unlike previous whiskbroom Landsat instruments, which have less than 150 detectors, the OLI is a pushbroom radiometer and, as such, has over 69,000 detectors covering the nine spectral bands. These detectors are arranged in the focal plane in 14 staggered Focal Plane Modules (FPMs), Figure 1. The number and location of the detectors has implications for the OLI radiometric calibration.

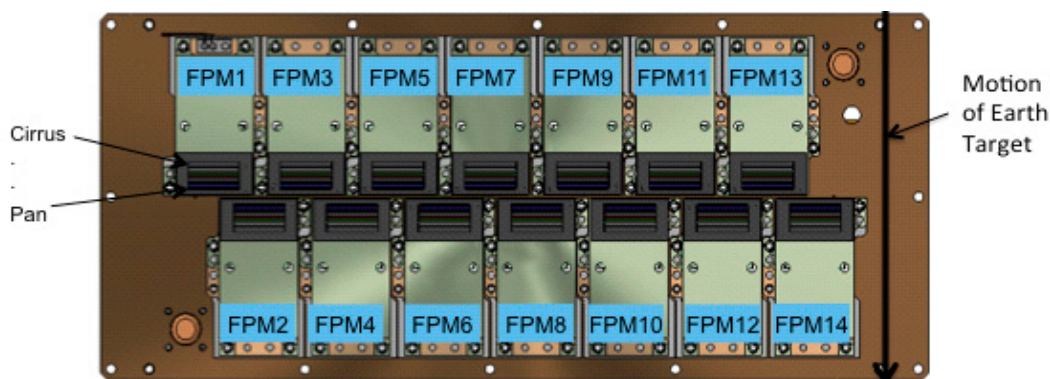
Table 1. The Operational Land Imager (OLI) Salient Characteristics.

Band (#)	Band Name	Center Wavelength (nm)	Bandwidth (nm)	IFOV (m)	Active Detectors (#)
1	Coastal-Aerosol (CA)	443	16	30	6916 (14 × 494)
2	Blue	482	60	30	6916
3	Green	561	57	30	6916
4	Red	655	38	30	6916
5	Near-IR (NIR)	865	28	30	6916
6	Short Wave IR-1 (SWIR 1)	1609	85	30	6916
7	SWIR 2	2201	187	30	6916
8	Panchromatic (Pan)	590	172	15	13,832 (14 × 988)
9	Cirrus	1373	20	30	6916

Key among the considerations in the design, build, test and operation of the OLI and the Landsat-8 system is providing data to the user community that is well understood and accurately referenced to standards of radiance ($\pm 5\%$, 1 sigma or $k = 1$) and reflectance ($\pm 3\%$, $k = 1$). These accuracies are achieved with a combination of factors including: (1) precision temperature control for the focal plane and focal plane electronics; (2) state of the art contamination control for all the optical surfaces, including the solar diffusers; (3) rigorous maintenance and validation of the radiance and reflectance scales as transferred from the national laboratories to the instrument and calibration devices; (4) a precisely maneuverable spacecraft to allow calibration using the sun and moon; (5) a concept of operations that includes

calibration observations on per-orbit, daily, weekly, quarterly and semiannual intervals, depending on the calibration type; and (6) an image assessment system to track the on-orbit performance of the system.

Figure 1. OLI focal plane showing 14 Focal Plane Modules (FPMs) and individual band spectral filters in their butcher-block assemblies.



In this paper we will review the calibration features built into the OLI instrument, summarize the pre-launch radiometric characterization and calibration of the instrument and then discuss its on-orbit performance in terms of radiometric stability across the mission to date. Comparisons to ground reference measurements and other satellites will be mentioned, but are discussed in more detail in other papers [2,3]. Aspects of the material included in this paper have been presented at a number of conferences [4–11].

2. OLI In-Flight Calibration Capabilities

The OLI has three primary radiometric calibration devices built into its hardware: (1) a shutter; (2) lamps; and (3) solar diffusers. Each of these devices is described in general in [1]. The lamps and solar diffusers will be discussed in more detail here. In addition, the Landsat-8 observatory routinely performs maneuvers that allow imaging of the moon by the OLI instrument (as well as TIRS).

2.1. OLI Data and Data Processing

In order to understand the OLI radiometric calibrators and absolute calibration, some background on the OLI data and data processing is required. OLI data are fundamentally 14-bit. During pre-launch testing all 14 bits were retained; on-orbit only 12 bits of the 14 bits are transmitted. For shutter (dark) data, the least significant bits are retained; for Earth and most calibrator data, the most significant bits are retained. All data are rescaled to 14 bits levels in initial ground processing [12] and converted to “real” data format. Earth and calibrator data are then “bias corrected” or converted to “net response”, by subtracting an average background value obtained from shutter data acquired before and after the calibration data. Next, the data are linearized based on a pre-launch determined Look-up-Table (LUT) [13], to provide “net-linearized response.” Selected calibrator data may additionally be converted to radiance by dividing by the detector responsivities. Earth data provided to users are rescaled to 16 bits and coefficients are provided in the data products to convert the data to top-of-atmosphere radiance or reflectance.

2.2. On-Board Lamps

A lamp assembly is located on each side of the OLI aperture stop, just behind the shutter assembly (Figure 2). Each assembly contains 6 five-watt tungsten halogen lamps. Each lamp in one assembly is wired in series with a lamp in the other assembly. Three pairs of the lamps operate off of the primary side of the instrument support electronics (ISE); the other 3 pairs are available if OLI is using the secondary side. A maximum of one pair can be powered at a time; any of the 3 pairs associated with the active power supply can be selected. Each assembly lamp pair is uniquely identified as “working”, “backup” or “pristine”, as defined by its usage frequency. An aluminized reflector within the lamp assembly along with a limited angle transmissive diffuser, direct the light through the OLI optics and onto the OLI focal plane. Neither lamp assembly alone is sufficient to illuminate the entire focal plane; however the full focal plane is illuminated by the combination of the two assemblies. The center part of the focal plane receives more light as both assemblies illuminate it (Figure 3).

Figure 2. (a) OLI lamp assembly drawing; (b) OLI lamp assemblies mounted on OLI aperture stop; (c) Calibration device locations in OLI optical path.

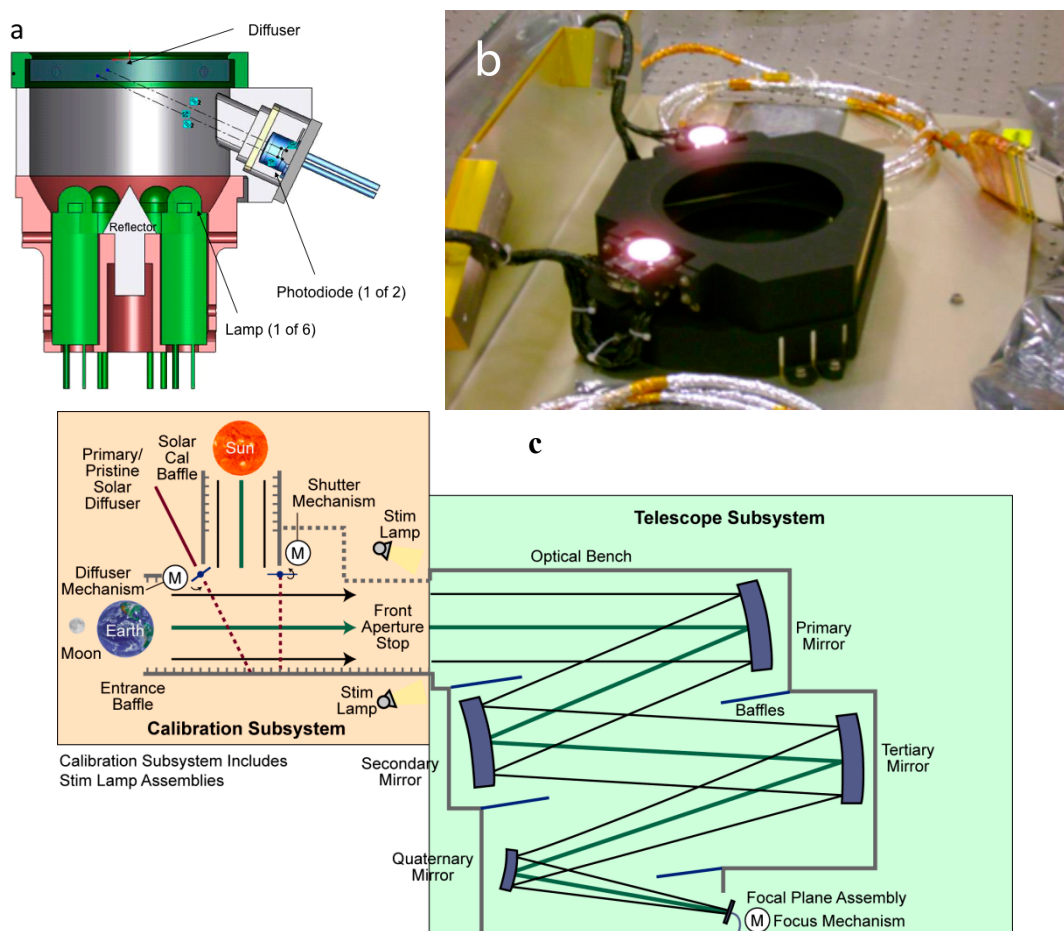


Figure 3. Working lamp pair illumination pattern on the OLI focal plane; (bias corrected and linearized average across 30 s after 2.2 min of warm-up). The discontinuities occur at the boundaries of the FPMs as the odd and even numbered FPMs are displaced relative to each other (Figure 1).

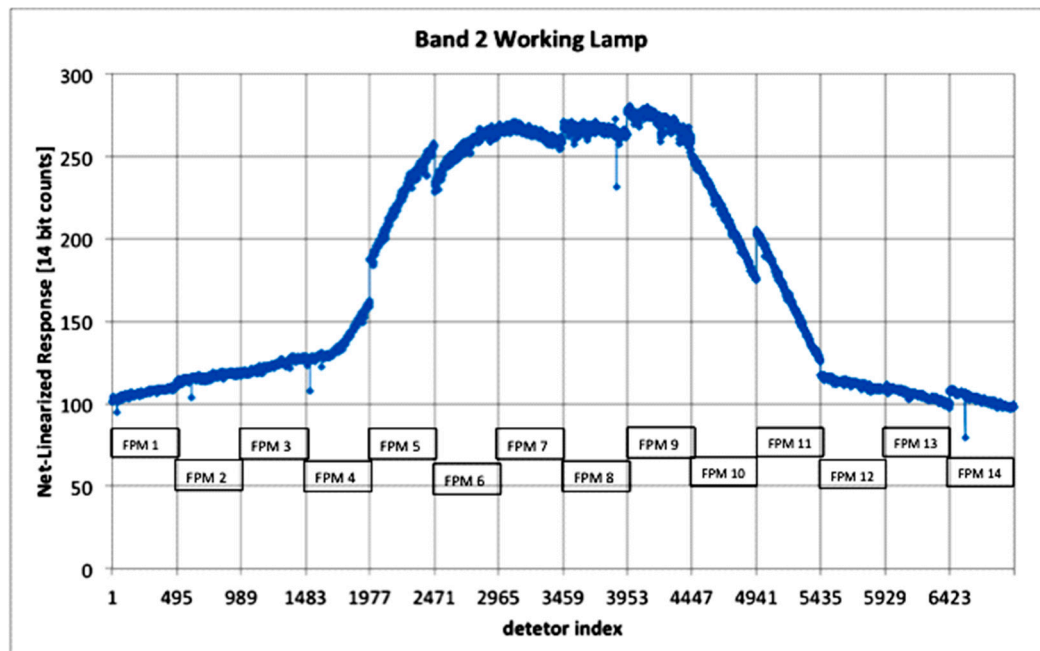
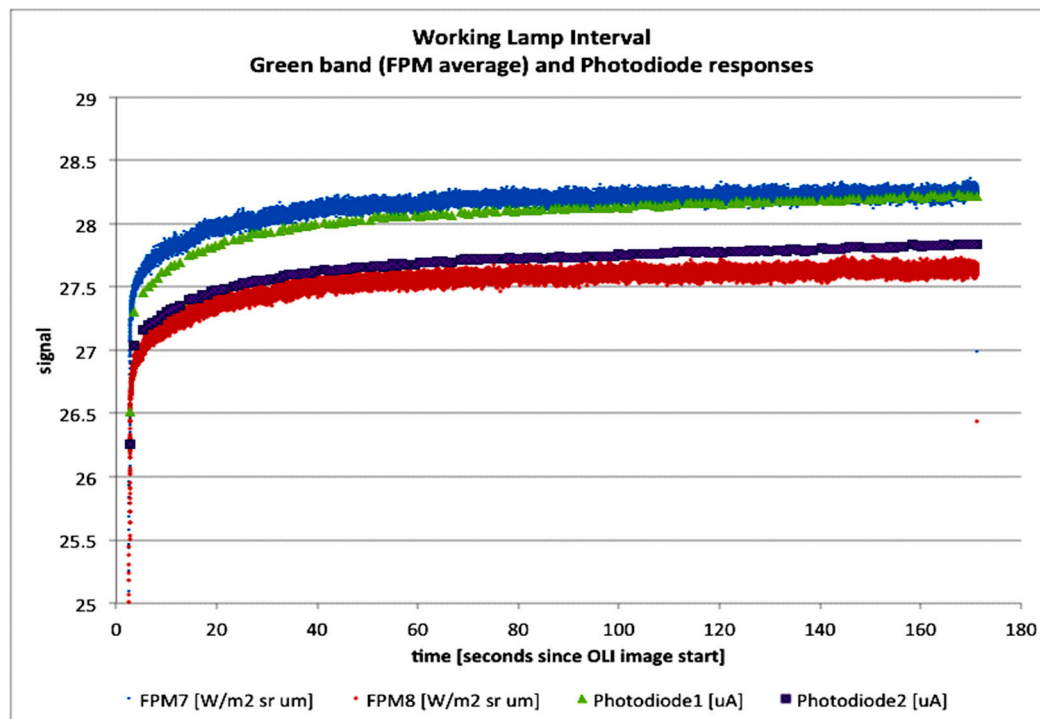


Figure 4. Warm-up behavior of the “working” pair of lamps as observed by the OLI detectors and monitor photodiodes during a pre-launch test. The OLI detector data are bias subtracted, linearized and converted to radiance, as described in Section 2.1.



A silicon photodiode filtered to receive light from 500 to 700 nm serves to monitor each lamp assembly’s output (Figure 2a); an additional pair of silicon photodiodes works when the secondary

power supply is used. The lamps are operated at a constant current of 1 A. Routine lamp telemetry includes: the power supply current, voltage for each lamp, current and temperature for each photodiode and temperature for each lamp assembly.

On-orbit lamp operations are as follows:

Close shutter (if not already closed), take dark measurement, start data acquisition, turn on lamp, wait 2.75 min, turn off lamp, stop data acquisition, take dark measurement. The normal on-orbit schedule is for the “working” lamp pair to be acquired once per day, the “backup” lamp pair every 16 days and the “pristine” lamp pair every six months. The different frequencies are to aid in separating lamp degradation from instrument degradation. Lamp acquisitions are usually on the ascending (night time) portion of the orbit to limit interference with normal Earth imaging. Prior to launch, lamp data were taken daily during instrument performance testing and at selected times during observatory level testing. For trending purposes a 30 s sample of data is extracted starting at 2.2 min after lamp turn on and averaged. An example of a lamp data acquisition from turn-on to turn-off is shown in Figure 4 along with the signals from the two photodiodes.

2.3. Solar Diffusers

The OLI includes a calibration assembly (Figure 5) at the front end of its optical system. Within the calibration assembly is the shutter that is used for dark measurements and the solar diffusers [1]. There are two solar diffusers in a wheel assembly along with an open aperture. Each diffuser is uniquely identified as “working” or “pristine” as defined by its operational usage. During normal imaging, the nadir port is pointed at the target (normally the Earth) and the open aperture is selected on the diffuser wheel. The solar diffusers are stowed at this time and protected from solar exposure. For a solar calibration, the solar port is pointed at the sun via a spacecraft maneuver, and one of the two diffusers is rotated into position. The solar diffuser is positioned at 45° to the optical axis, such that the long dimension of the diffuser corresponds to the cross track direction of the focal plane. When illuminated by the sun down the solar port, the illumination vector and the detector lines of sight are nearly (~ 1 degree) co-planar. As such, the OLI detectors nearest the optical axis observe the diffuser at near the specular angle (45°) whereas the detectors at the end of the focal plane are at angles about 7.5° larger or smaller (52.5° or 37.5°).

Each solar diffuser is made of space-grade Spectralon[®], a sintered Polytetrafluoroethylene (PTFE) product produced under conditions that limit contamination with hydrocarbons that can lead to reflectance degradation with ultraviolet exposure. Reflectance testing of witness samples prior to launch before and after UV exposure was used to confirm the material purity.

A normal solar diffuser acquisition is as follows: close shutter; maneuver spacecraft to align sun with solar port and track sun, take dark data, deploy diffuser, open shutter, take diffuser data, close shutter, stow diffuser, take dark data, return spacecraft to normal Earth pointing mode. One diffuser, designated “working”, is deployed about every 8 days. The other diffuser, designated “pristine”, is used about every 6 months to help track any degradation in the working diffuser. A normal solar collect is 500 multi-spectral lines of data (2.2 s); though 60-s collects are taken semi-annually. The actual diffuser exposure time is about 60 s more than the data acquisition time. The OLI data are corrected as discussed in Section 2.1, averaged over time and adjusted for the OLI-Sun distance at the time of the acquisition

for stability trending purposes. Additional processing for a reflectance-based calibration is described in Section 6. Data from a sample solar diffuser collect is shown in Figure 6. Most of the variation in Figure 6 is due to responsivity differences between the various detectors and focal plane modules.

Figure 5. Components of the calibration assembly.

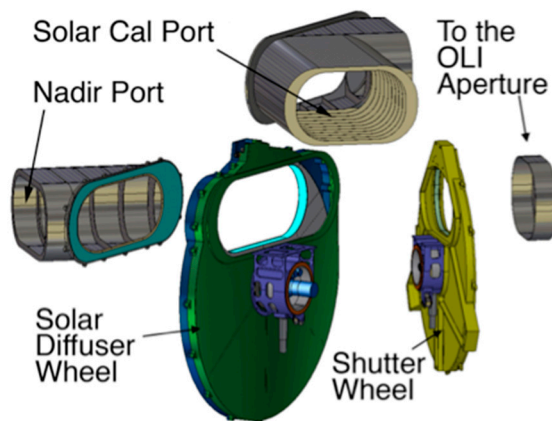
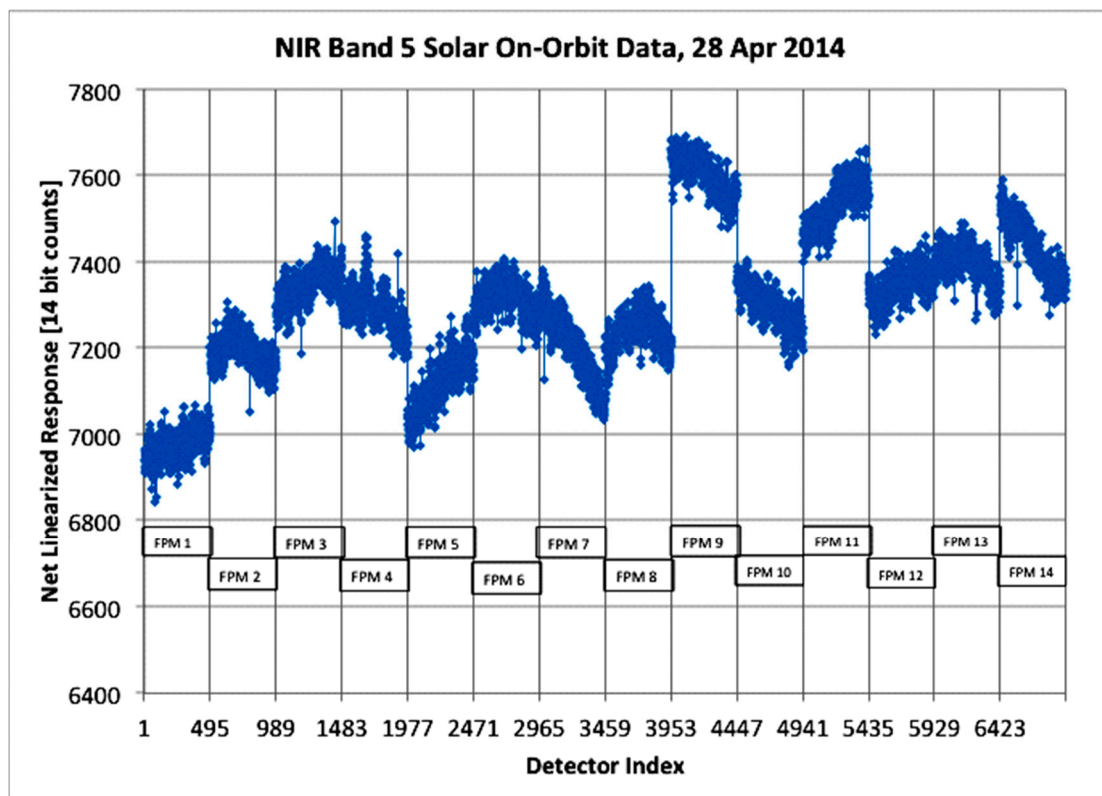


Figure 6. “Working” Diffuser On-Orbit Data for 28 April 2014, NIR band.



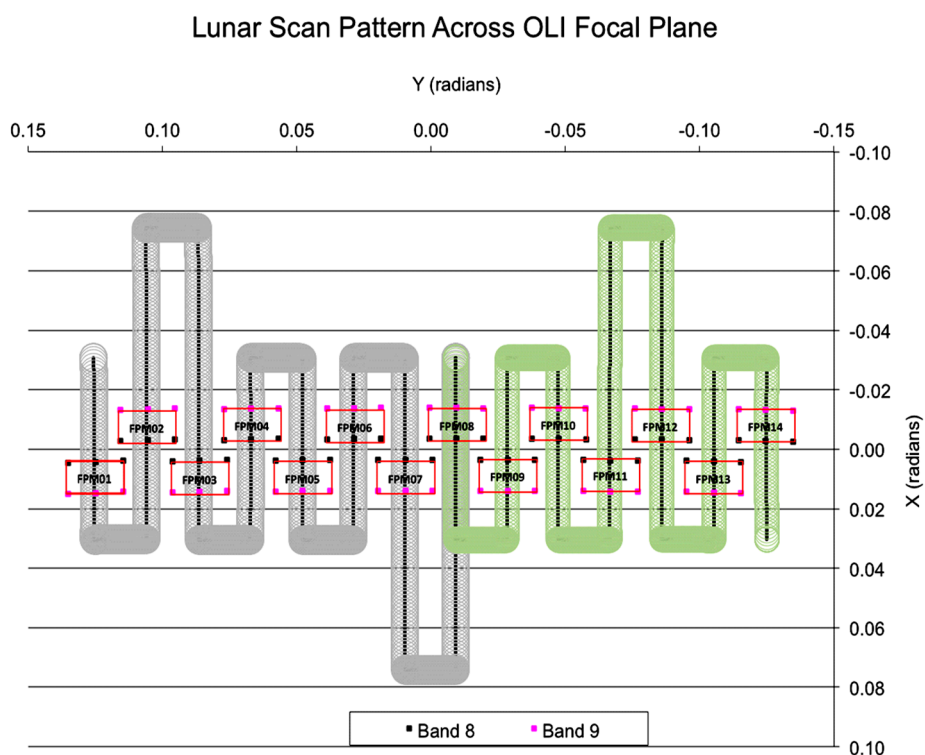
2.4. Lunar Calibration

The moon is an extremely stable reflector of sunlight, and when the angle and extent of solar illumination visible by the satellite instrument is properly accounted for, an effective source for trending radiometric performance [14–17]. Most satellite sensors that use the moon as a calibration source rely on the lunar irradiance model developed at USGS [18] based on observations by the RObotic Lunar

Observatory (ROLO). This model provides lunar disk irradiances for all the OLI wavelengths at any given time as observed from a given location when the lunar phase angle is between -90 degrees and $+90$ degrees. In order to use this model, the sensor must image the full lunar disk and the signal must be integrated across the disk. As the OLI is a pushbroom imager whose line of sight is fixed relative to the spacecraft, in order to create a lunar image, the spacecraft must point OLI to the moon with dedicated maneuvers.

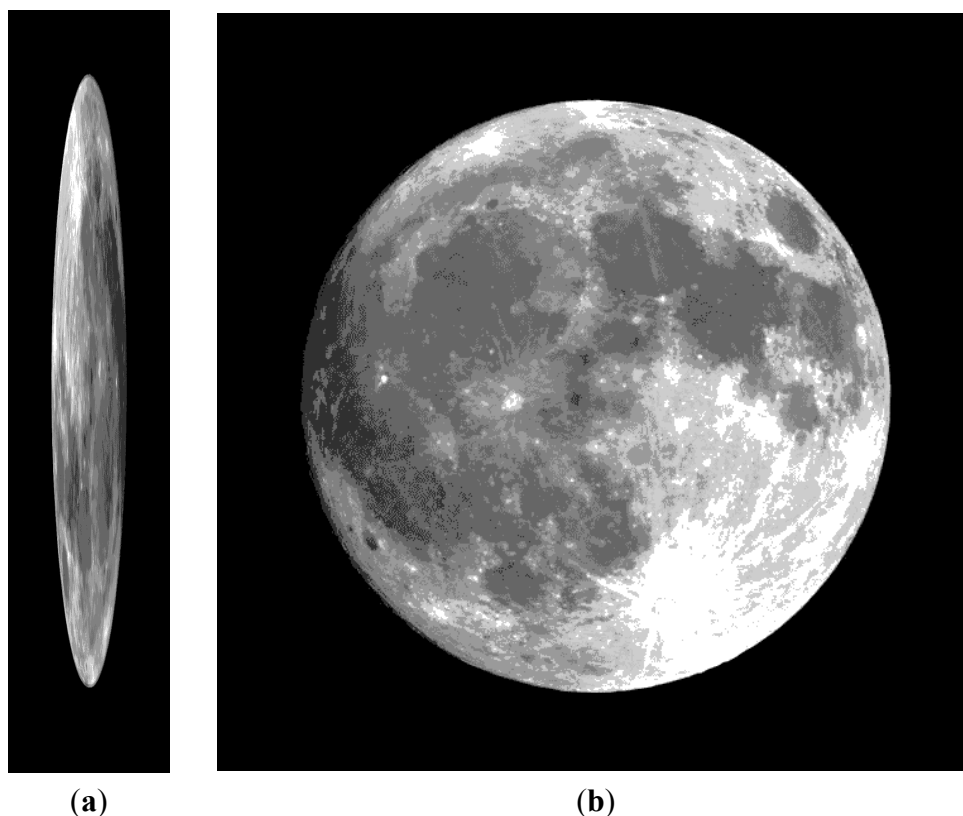
The lunar scanning pattern selected for Landsat-8 allows for each FPM to image the moon. On even number months within the range of $+5^\circ$ to $+9^\circ$ lunar phase angle, the spacecraft slews to point the OLI near the moon during the Earth eclipse part of the orbit. Starting with FPM 8, the spacecraft maneuvers to scan each FPM down to FPM 1, as shown in Figure 7. Image data are recorded during the pure pitch portions of the maneuver from one lunar diameter off the moon on one side to one lunar diameter off the moon on the other side. The maneuver is designed to maintain the angular velocity of the pitch as constant as possible during the imaging portion of the maneuver to reduce radiometric uncertainties in the lunar irradiance due to image distortion; better than $\pm 1\%$ was obtained. The spacecraft slews back to point the instruments at the Earth for the daylight pass and, during the next Earth eclipse, slews back to the moon to complete the scanning pattern from FPM 8 to 14. The extended scans, e.g., after FPM 3 and before FPM 2, are to allow TIRS imaging of the moon. The $\sim 0.5^\circ$ lunar extent fits well within each FPMs $\sim 1.1^\circ$ field of view. On odd months the same phase angles are used, but the pattern is altered so that FPM 7 images the moon first followed by the higher number FPMs on the first orbit; on the second orbit FPM 7 is again imaged first, followed by the lower number FPMs.

Figure 7. The OLI scan pattern of the moon over two orbits on even number months (gray is orbit #1; green is orbit #2). The center and edge detectors show the extent of each FPM in the outer and inner bands (bands 8 and 9).



The pitch rate used during the image acquisition results in a factor of 8 oversampling in the along-track direction (Figure 8a). The current lunar processing procedure uses the radiometrically corrected lunar products, that is, bias-subtracted, linearized and converted to radiance. Inputs to the USGS lunar irradiance model for each observation include the spacecraft position, time of acquisition and the apparent (oversampled) along-track size of the lunar disk. Currently, the OLI integrated irradiances are obtained by summing up all the lunar pixels above a threshold value of 1 percent of the maximum pixel value in each image. An image mask created from this threshold is used to estimate the along track diameter of the moon as well as the position (and hence the time) of the moon center in the image. The latter is used together with information from the spacecraft ancillary data to obtain the spacecraft position in J2000 reference frame. Ratios of the instrument irradiances *versus* the modeled values are then used for further analysis. A sample geometrically corrected lunar image is shown in Figure 8b.

Figure 8. OLI Lunar Images, Pan band, 26 March 2013, FPM 7. (a) Level 1R; (b) Level 1G, radiometrically and geometrically corrected (enlarged $\sim 8\times$ relative to (a)).



3. OLI Pre-Launch Radiance Calibration and Stability Monitoring

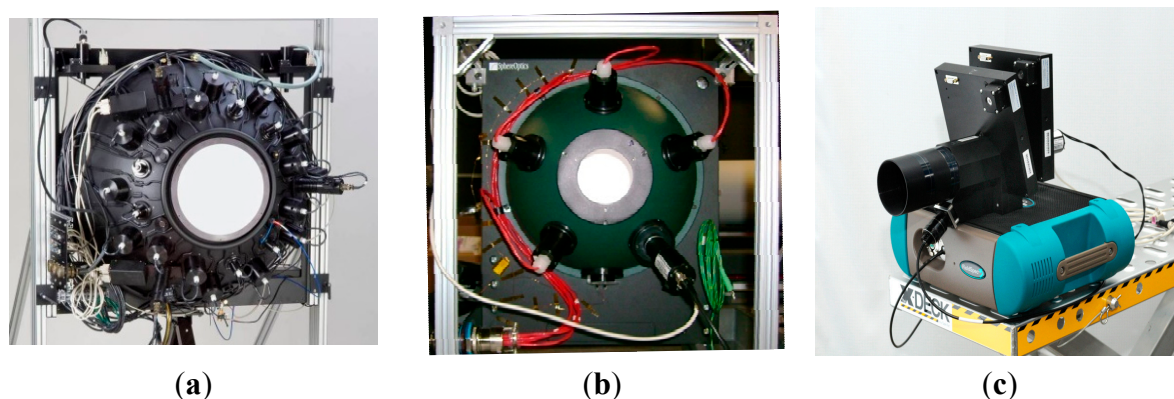
3.1. Absolute Radiance Calibration

The OLI instrument underwent extensive pre-launch characterization and calibration testing at BATC [1]. Key aspects of the radiometric testing were to characterize the stability of and assign an absolute radiometric scale to the OLI instrument. The primary radiometric source for this testing was a large aperture integrating sphere, a.k.a., the Death Star Source (DSS) [6]. The DSS (Figure 9a)

provided up to full-scale radiance in all of the OLI bands. The radiometric scale of the DSS was maintained via internal detectors that use OLI witness sample filters. These detectors were used to set the source radiance through a feedback loop.

An overview of the DSS radiance scale derivation process is illustrated in Figure 10a,b. The DSS radiance scale was obtained by transfer via two intermediary BATC artifacts: a Small Sphere Source (SSS) and the COTS Transfer Radiometer (CXR) (Figure 9b,c). The SSS was calibrated at the NIST Facility for Spectro-radiometric CALibrations (FASCAL) (Figure 10a). While still at NIST the SSS was characterized using the Ball Standard Radiometer (BSR) [6], the University of Arizona VNIR and SWIR Radiometers [19,20], the Landsat Transfer Radiometer (LXR) [20], the NIST Visible Transfer Radiometer (VXR) [20] and other commercial spectrometers owned by NASA, University of Arizona and NIST. The BSR is a filter radiometer that covers the full spectral range of the OLI instrument. The CXR is similar to the BSR with an attached spectrometer to give the full spectral structure across the same wavelength range. After transport to BATC, the SSS was rechecked with the BSR. Subsequently the SSS calibration was transferred to the CXR. The CXR calibration was transferred to the DSS internal monitors by having the CXR view the DSS through the vacuum chamber (CALibration Test Set–Radiometric Calibration (CATS-RC)) window through which OLI would observe the DSS (Figure 10b). This calibration was then transferred to the OLI instrument with the OLI (under vacuum) viewing the DSS through this window. After the OLI calibration was completed, the calibrations of the SSS, DSS, and CXR were revalidated by comparisons to the UA XR's, LXR, and VXR (Figure 10a) and aforementioned spectrometers.

Figure 9. Ball Aerospace & Technologies Corp (BATC) artifacts used for OLI calibration: (a) Death Star Source; (b) Small Sphere Source; (c) COTS Transfer Radiometer (CXR).



The radiometer measurements of the SSS indicated that this sphere decreased in output at the shorter wavelengths as a function of lamp usage. This change amounted to $\sim 1.5\%$ in the OLI CA band between the time the SSS was calibrated at FASCAL and subsequently used to calibrate the CXR at BATC. Because of this change, the procedure was modified to keep the radiance scale with the CXR instead of the SSS, adjusting the CXR scale for the changes observed in the SSS. The independent validations of the DSS radiance scale using the UAR's, LXR, *etc.* indicated that the DSS radiances were generally within their uncertainty bounds ($\sim 2\%$, $k = 1$) [10] with the possible exception of the region in the vicinity of the OLI band 7, that was about 3% lower than the validating radiometer (Figure 11).

The OLI radiance calibration, as indicated, was performed with the OLI under vacuum conditions and the DSS source outside of the chamber. The OLI was pointed to center each FPM on the sphere aperture during these calibrations. At the high (near full scale) radiance for each band, the uniformity across of source was within $\pm 0.1\%$ for all but the SWIR2 band, which was about $\pm 0.25\%$. The estimated uncertainty of the OLI radiance calibration prior to launch is $\sim 2.5\%$ ($k = 1$).

Figure 10. (a) Radiance traceability flow from NIST to BATC: (1) Calibration of the Small Sphere Source (SSS) by FASCAL at NIST; (2) Transport of SSS from NIST to BATC with checks by the Ball Standard Radiometer (BSR), University of Arizona radiometers (UAR's) and government (NIST and NASA) radiometers before and after transport; (3) Transfer of the calibration from the SSS to the COTS Transfer Radiometer (CXR) by measurements at BATC. The Spectral Irradiance and Radiance responsivity Calibrations using Uniform Sources (SIRCUS), a NIST facility [21], was used to provide the CXR spectral response. The NIST Portable Radiometric Source (NPR) [18] provided an additional check on the stability of the radiometers; (b) Radiance traceability flow from BATC to on-Orbit: (4) Calibration of the Death Star Source (DSS) by the CXR through the CATS-RC chamber window; (5) Calibration of the OLI instrument in the CATS-RC chamber; (6) Transfer of calibration to the illuminated flight diffusers with the heliostat in CATS-RC; (7) Recalibration of the OLI by the solar illuminated diffuser on-orbit; (8) Observations of the Earth by the OLI.

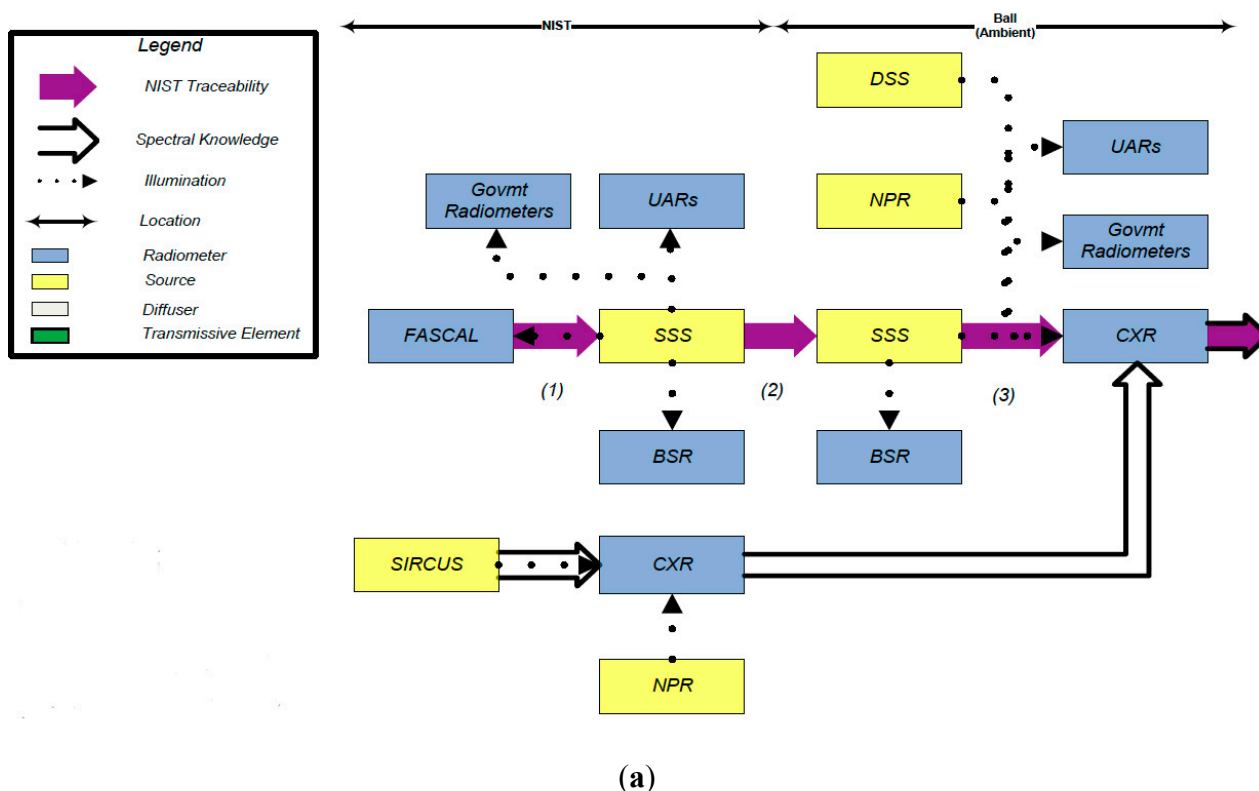


Figure 10. Cont.

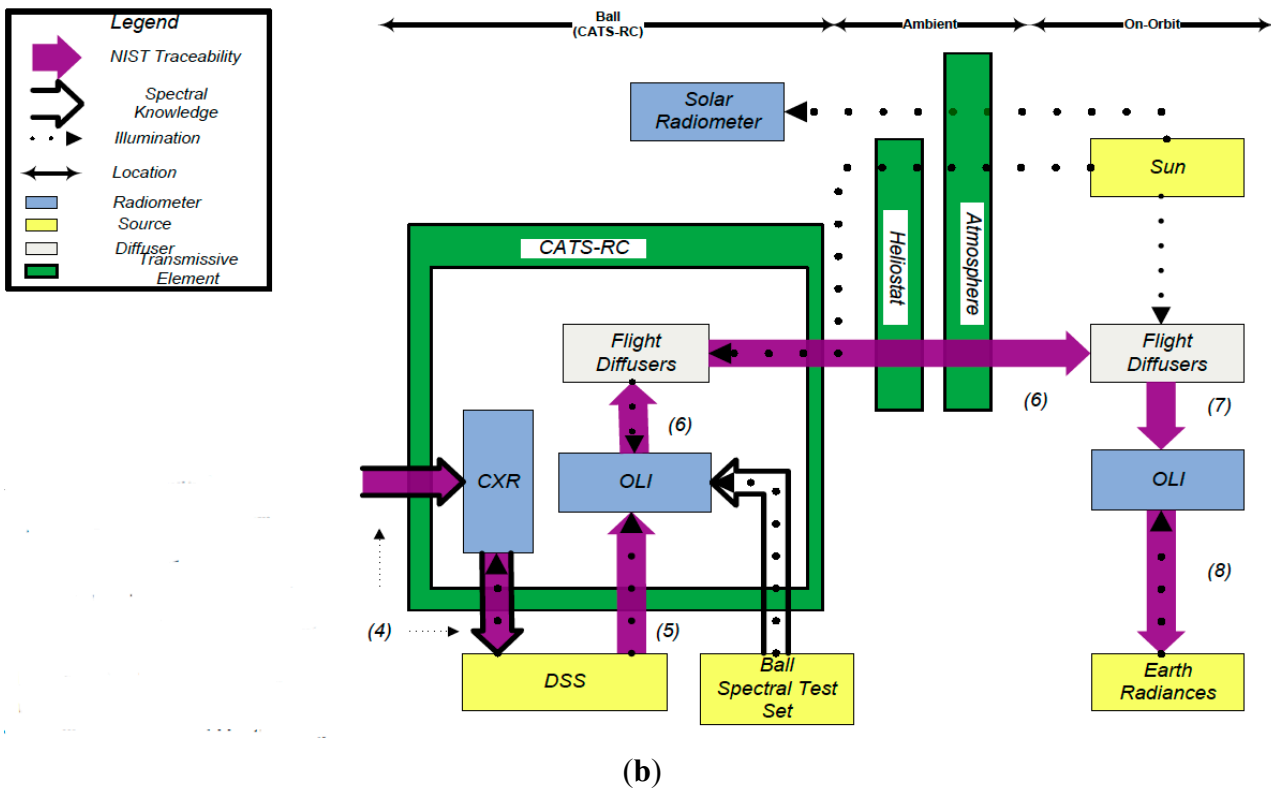
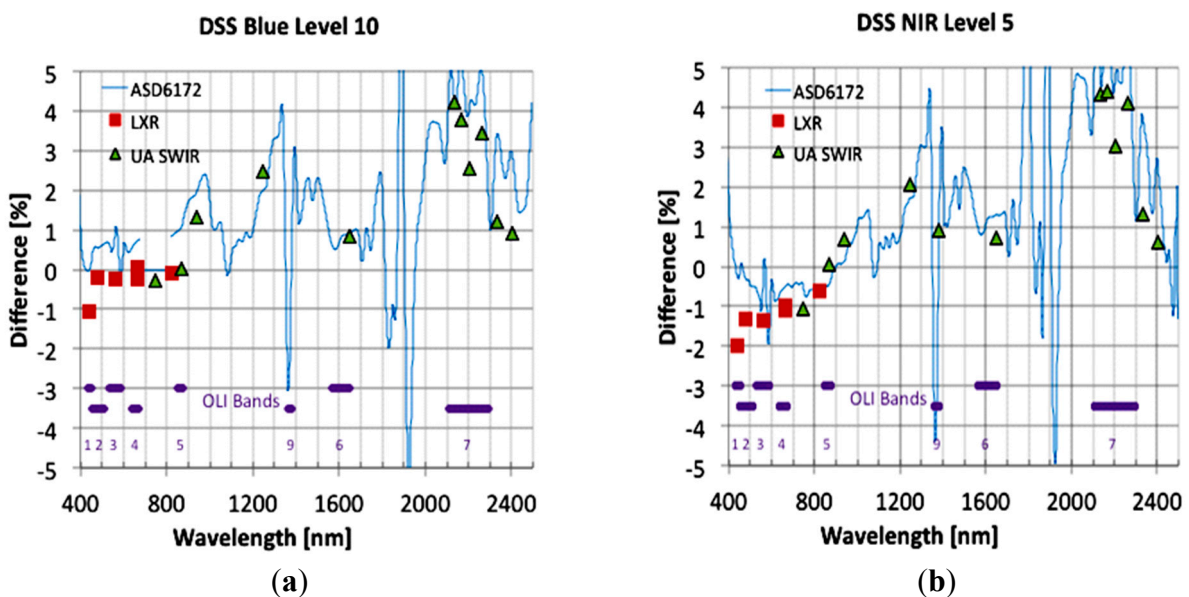


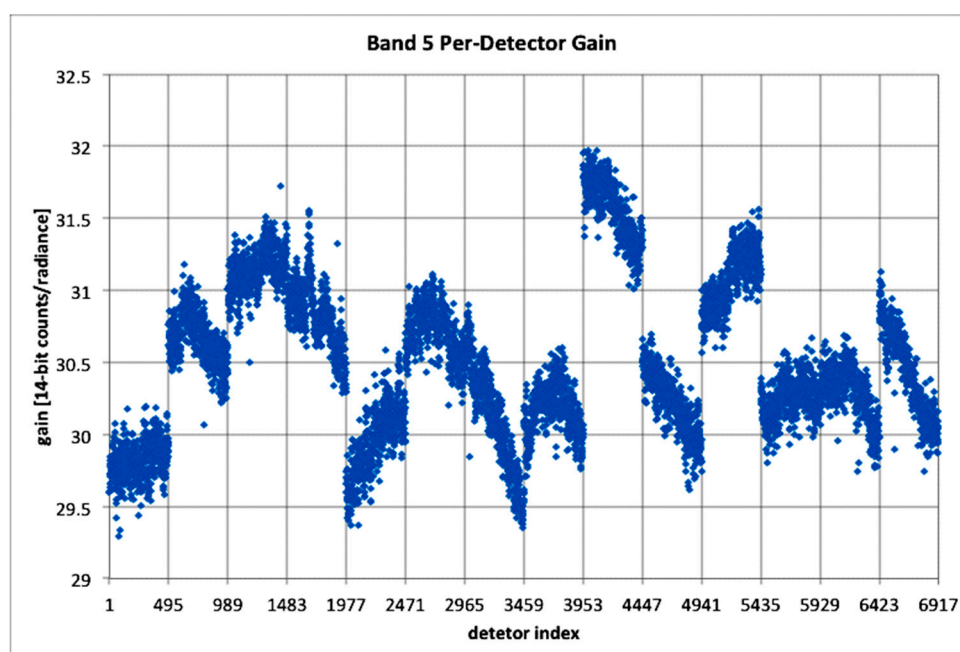
Figure 11. (a,b) Validations of the BATC DSS radiance scale by comparison to NASA and University of Arizona radiometers. One spectrometer (ASD6172) and two of the participating radiometers (LXR, UA SWIR) are shown. Two DSS radiance levels are shown, where the band, e.g., “blue”, designates the control wavelength and the “Level” is a brightness designation, with Level 10 being the brightest.



The OLI was tested at 41 different radiance levels, though the absolute calibration of each band was based on one sphere level near the high end of the OLI dynamic range. This level was controlled in the

feedback loop by the internal DSS detector filtered with an OLI witness filter for the same band. The original plan was to use multiple sphere levels controlled at various wavelengths and perform a regression to obtain the responsivity; however, the radiances were less repeatable at wavelengths other than the control wavelength [10]. The OLI responsivities (gains) were derived by dividing the net linearized OLI response by the OLI relative spectral weighted radiances of the DSS Level 10 (Figure 12). These pre-launch gains were the initial gains stored in the Calibration Parameter File (CPF) for use by the Landsat Product Generation System (LPGS); the gain values provided in the CPF are contained in two fields: OLI_ABSOLUTE_GAINS, which are averages for each focal plane module and OLI_RELATIVE_GAINS, which are individual detector values referenced to each FPM average. The CPF's are available online [22].

Figure 12. OLI radiance responsivity (bias corrected, linearized, 14 bit counts/(W/m² sr μm) for all OLI NIR (Band 5) detectors based on NIR sphere Level 10).



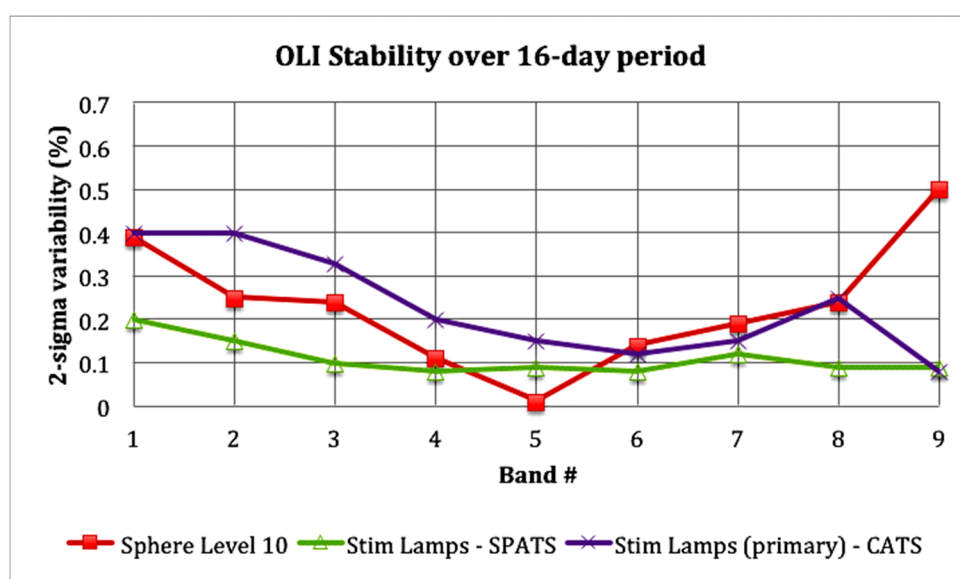
3.2. Radiometric Stability

The OLI radiometric stability was evaluated relative to two sources and over several time scales during pre-launch testing. Certain DSS sphere levels were repeated over the multiple days of CATS-RC testing. In addition, a working OLI stim lamp collect was taken daily during thermal vacuum testing at the instrument level, *i.e.*, during the radiometric (CATS), SPAtial Test Set (SPATS) and the Thermal Vacuum Thermal Balance (TVTb) testing, and at the integrated observatory level. Over a 16-day period (corresponding to one on-orbit repeat of the WRS-2 cycle), the OLI band average responses varied by less than 0.5% ($k = 2$) during multiple tests (Figure 13). Note that this is the combined stability of the source and the instrument, so the instrument itself is at least this good.

The response of the OLI to the stim lamps over the full pre-launch test period is illustrated in Figure 14a for selected FPM's of the Panchromatic band, indicating about a $\pm 2\%$ variation in response over this period. To understand what portion of this variability is instrument related, it is necessary to understand two aspects of the stim-lamp geometry and radiometry. First, the two stim lamp assemblies

(labeled A and B) illuminate the focal plane; each FPM receives a different amount of light from each assembly. The high numbered FPMs (#14 shown) are illuminated only by assembly A; the low number FPMs (#1 shown) by assembly B; the intermediate number FPMs (#7 and #8 shown) by both. Second, the OLI orientation was changed to accommodate each different test environment. In turn, each orientation changed the direction of the gravitational force relative to the lamp filaments. On day 0 during SPATS, the OLI mounting feet were down; around day 70 during CATS, the feet were up; around day 220 during Thermal Vacuum Thermal Balance (TVTB), the feet were down; and around day 740 during observatory level testing, the feet were to the side. Note that SPATS and CATS were instrument performance test periods, whereas the other periods were environmental tests, where conditions, particularly temperature, were intentionally cycled.

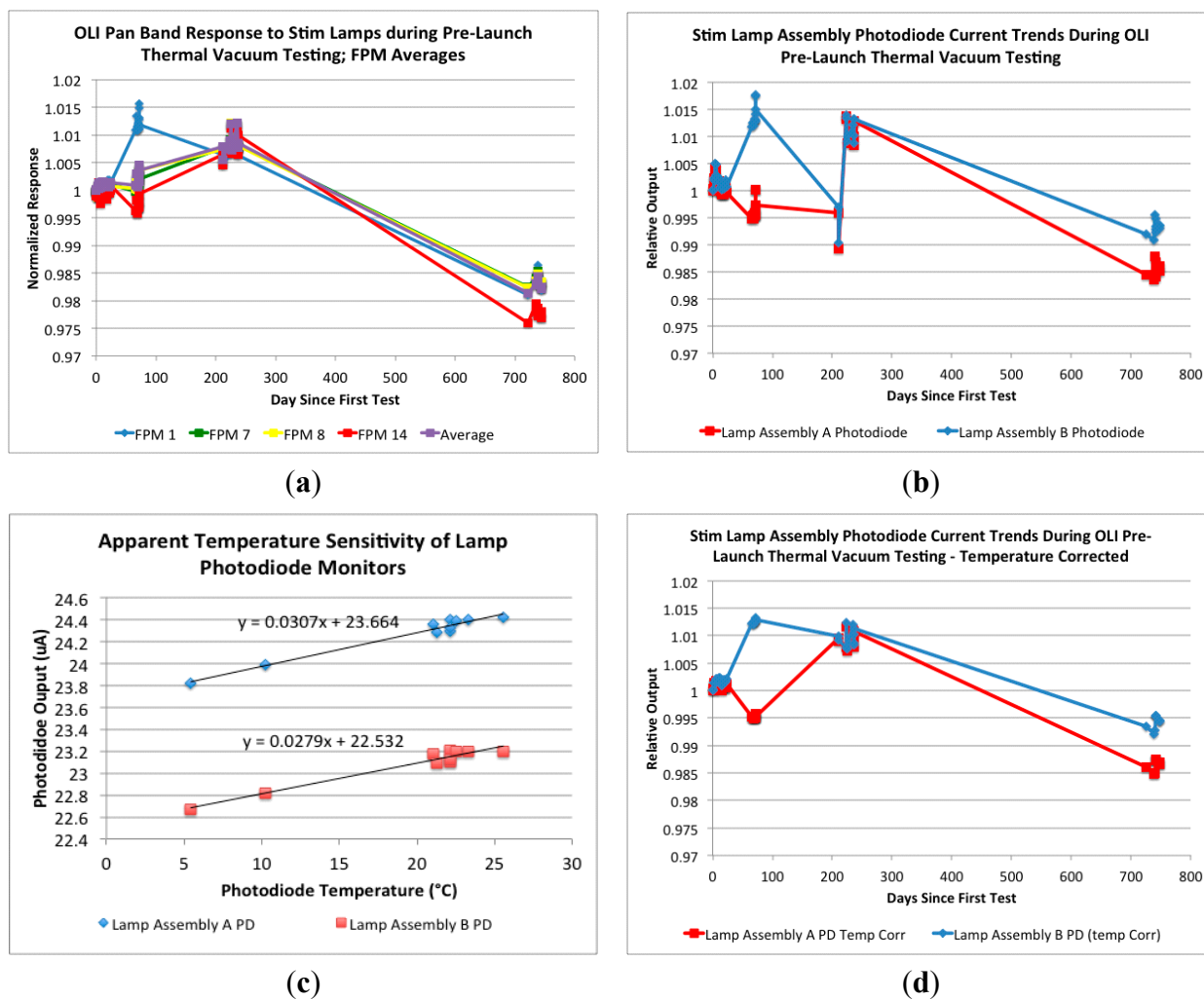
Figure 13. OLI radiometric stability over a 16-day period using different sources.



The OLI stim lamp assemblies, as indicated, have several built in monitors that can be used aid in understanding whether the response variation observed in Figure 10a is the OLI or the lamp. During prelaunch testing, the monitor measuring current to the lamp remained constant to within $\pm 0.02\%$. The internal photodiodes, which are filtered to approximately the same wavelength range as the pan band, showed divergent behavior of the two lamp assemblies, particularly in going from SPATS (first group of points from day 0 to ~ 30) to CATS (second group of points around day 80) (Figure 14b). This is hypothesized to be due to the aforementioned change in the OLI orientation, hence the gravitational influence on the lamp filaments. The OLI response to the stim lamps (Figure 14a) generally mirrors the internal photodiode responses (Figure 14b), with the exception of two outlier points around day 220 that were depressed in the photodiodes, but not in the OLI response. These two points represent data taken when the lamp assemblies were at 10°C and 15°C , outside of the normal 23° to 30°C range. The photodiode response as a function of temperature for the TVTB test setup is presented in Figure 11c. This shows a temperature sensitivity of about $0.1\%/^\circ\text{C}$. Evidence of this temperature sensitivity is also seen in the warm-up behavior of the lamps (Figure 4), where the OLI response to the lamps flattens out more quickly than the photodiodes with time, as the lamp assembly warms up. Correcting for this temperature sensitivity gives Figure 14d, which removes the outliers. FPM 1 which receives light from

only lamp assembly B, matches the lamp B photodiode better and FPM 14 tracks the lamp A photodiode better. As can be observed by comparing Figure 14a,d, up until the final test, the OLI pan band response tracked the photodiode response to within a few tenths of a percent. In the final test the OLI response was about 1% lower than the photodiode, so at most there was a 1% shift in the OLI pan band response.

Figure 14. OLI radiometric response to working lamp during thermal vacuum testing. (a) Pan band response; (b) Photodiode response; (c) Photodiode Temperature Sensitivity; (d) Temperature Corrected Photodiode Response.

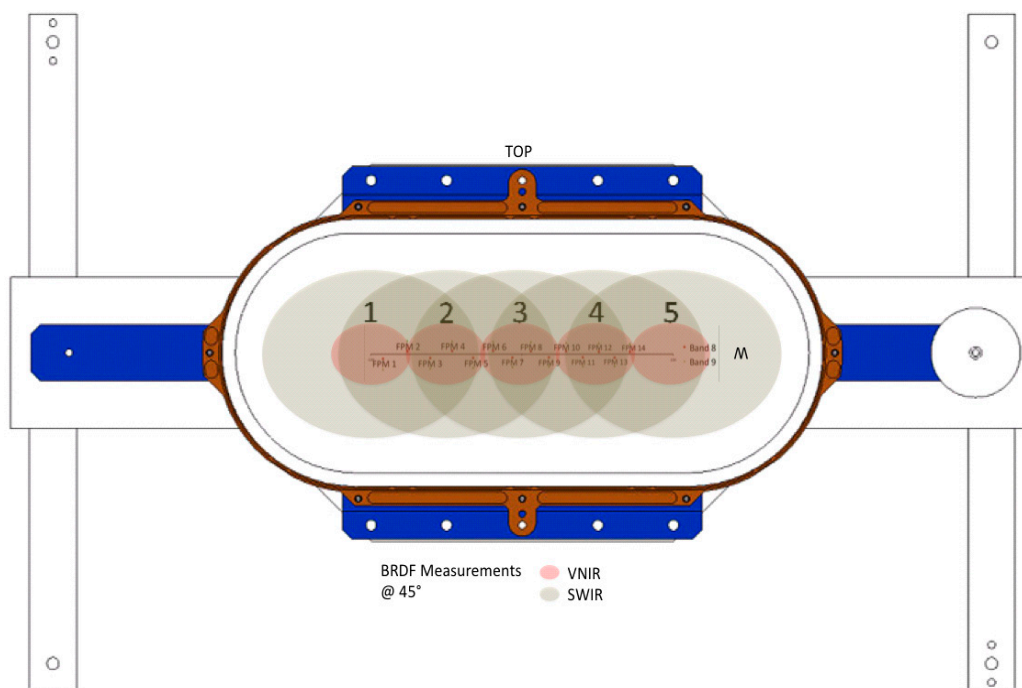


The OLI green and red bands, which are spectrally within the panchromatic band, showed a similar variation to the panchromatic band, *i.e.*, $\pm 2\%$ without correcting for the lamp variation (like Figure 14a). For the shortest wavelength CA band the variation was $\pm 4\%$ and the longest wavelength SWIR 2 band, $\pm 0.5\%$. These variations are spectrally consistent with lamp behavior, *i.e.*, largest at the shortest wavelengths. Like the panchromatic band, were data available to correct for the lamp output, these magnitudes would be reduced.

4. OLI Pre-Launch Reflectance Calibrator Characterization

As described above, the OLI calibration subassembly houses two Spectralon solar diffusers. Prior to launch, the bidirectional reflectance properties of these diffusers were characterized across the range of OLI detector view angles for the 45° solar incidence angle at which they are illuminated on-orbit [9]. The reference standard for this characterization was a Spectralon diffuser (25 × 25 cm) that had been measured at the NIST Spectral Tri-function Automated Reflectance Reflectometer (STARR) facility [5]. Bidirectional Reflectance Factors (BRFs) of this standard were measured for the 0° illumination/45° view angle condition, from 400 to 2500 nm at 25 nm intervals; 45° illumination/−45° view angle condition from 400 to 1100 nm at 25 nm intervals, plus 1375 nm, 1610 nm and 2200 nm; and 45° illumination/−37.5° to −52.5° every 7.5° view angle conditions at 665 nm and 1610 nm. The NIST stated uncertainty for these measurements from 400 to 2300 nm was ~0.33% ($k = 1$) [5].

Figure 15. OLI diffuser in holder for reflectance measurement. The five measurement locations and approximate fields-of-view of the radiometer are shown in relation to the centers of fields of view of the OLI detectors on the FPMs 1–14.



The flight diffuser characterization was performed at the University of Arizona's College of Optical Sciences Remote Sensing Group goniometric laboratory [9]. The BRFs were measured at five locations on the diffuser (Figure 15) that cover the range of area viewed by the OLI detectors. OLI spectral filter witness samples were used to define the spectral bandpasses. Wavelengths below 1000 nm were measured with the UA VNIR radiometer; those above 1000 nm with the UA SWIR radiometer [17,18]. At the five locations measurements were taken with 45° illumination and −37.5° to −52.5° every 7.5° in view angle, at 0° and ±2° out of plane. The fields of view of the two radiometers were different; the approximate fields of view for the −45° view condition are shown in Figure 15. The estimated uncertainty in the measurements varies from 1.1% at 630 nm to 1.9% at 2200 nm ($k = 1$). Sample results at three wavelengths are presented in Figures 16 (working diffuser) and 17 (pristine diffuser).

Figure 16. OLI working diffuser Bidirectional Reflectance Factors: Row 1: (a) In-plane, 445 nm, all positions; (b) Varying azimuths, 445 nm, position 3; Row 2: (c) In-plane, 863 nm, all positions; (d) Varying azimuths, 863 nm, position 3; Row 3: (e) In-plane, 2206 nm, all positions; (f) Varying azimuths, 2206 nm, position 3.

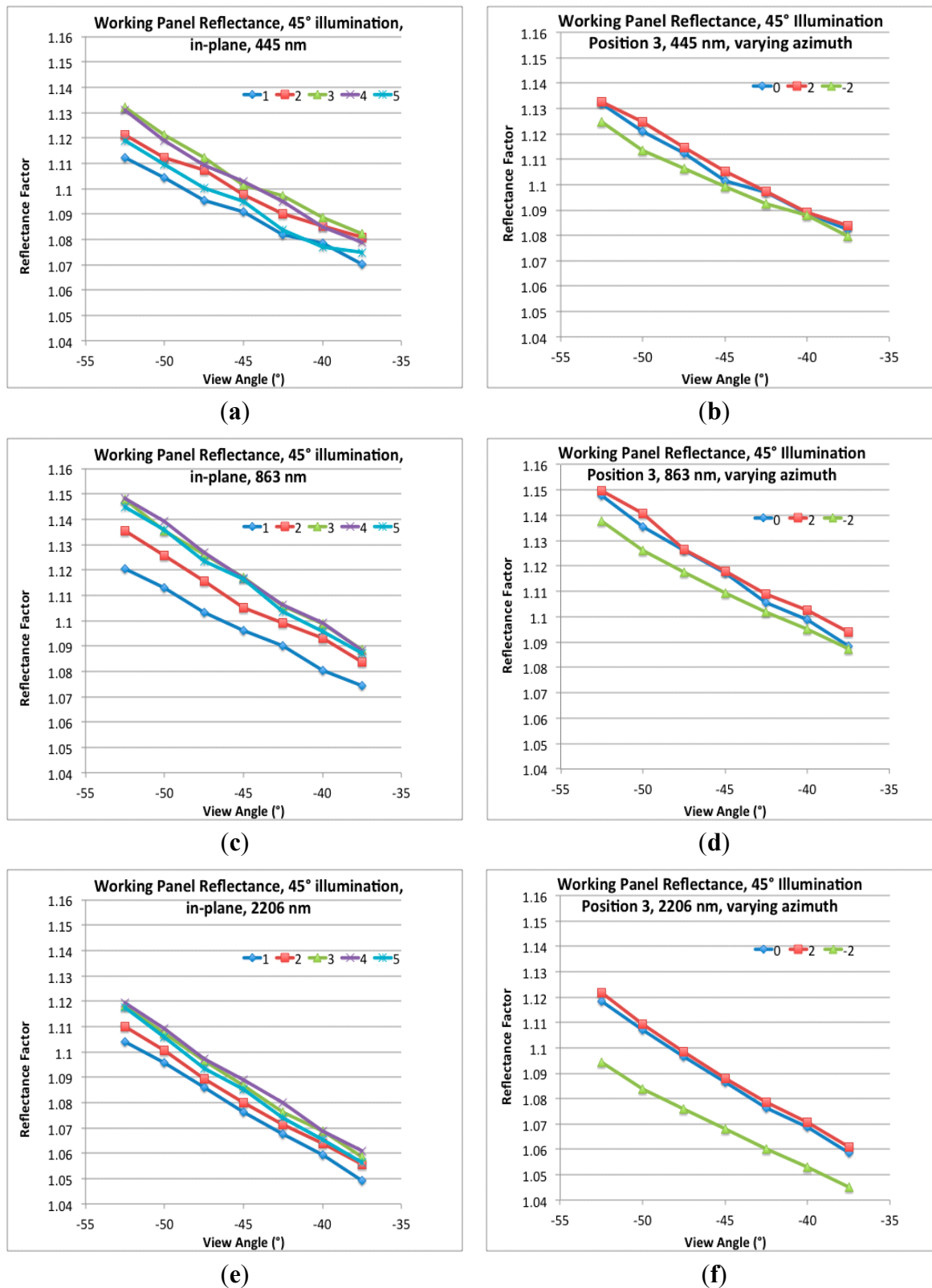
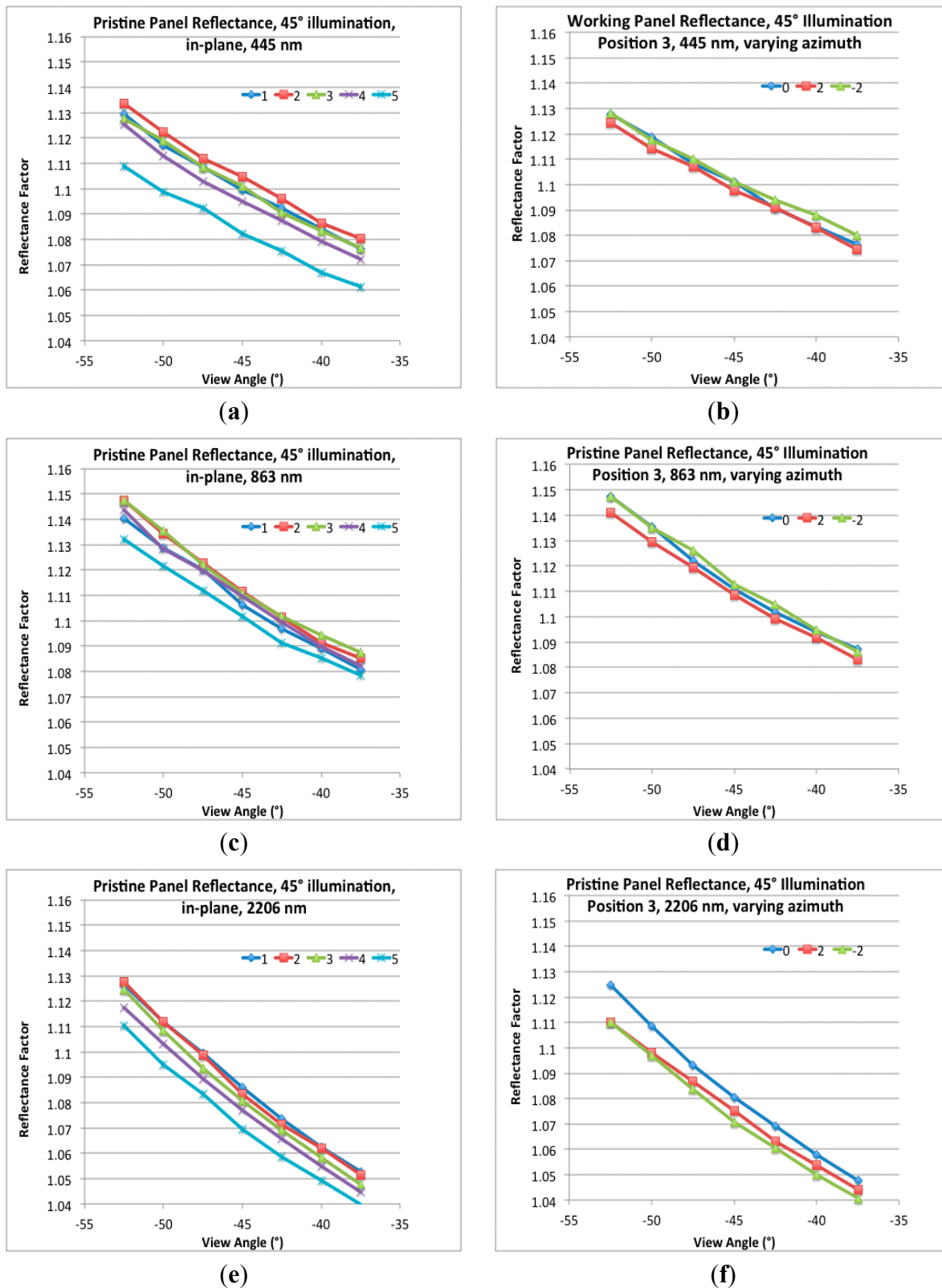


Figure 17. OLI pristine diffuser Bidirectional Reflectance Factors: Row 1: (a) In-plane 445 nm, all positions (b) Varying azimuths, 445 nm, position 3; Row 2: (c) In-plane, 863 nm, all positions; (d) Varying azimuths, 863 nm, position 3; Row 3: (e) In-plane, 2206 nm, all positions; (f) Varying azimuths, 2206 nm, position 3.



The two panels are similar in their reflectance properties, with all five locations on each panel within an envelope of $\pm 1\%$ reflectance. The slopes of the two panels with view angle are also similar, changing about 5%–7% in reflectance from -37.5 to -52.5° . A few differences worth noting: (1) location 1 on the working panel is on the low side in terms of reflectance relative to the rest of the locations, whereas it is location 5 on the pristine panel that is the lowest; (2) there appears to be an asymmetry around the principal plane in the working panel that is less evident in the pristine panel and (3) the view angle dependence is larger in the pristine panel at 2206 nm, changing by about 8% *versus* 6% for the working panel.

Figure 18. BATC heliostat test facility.

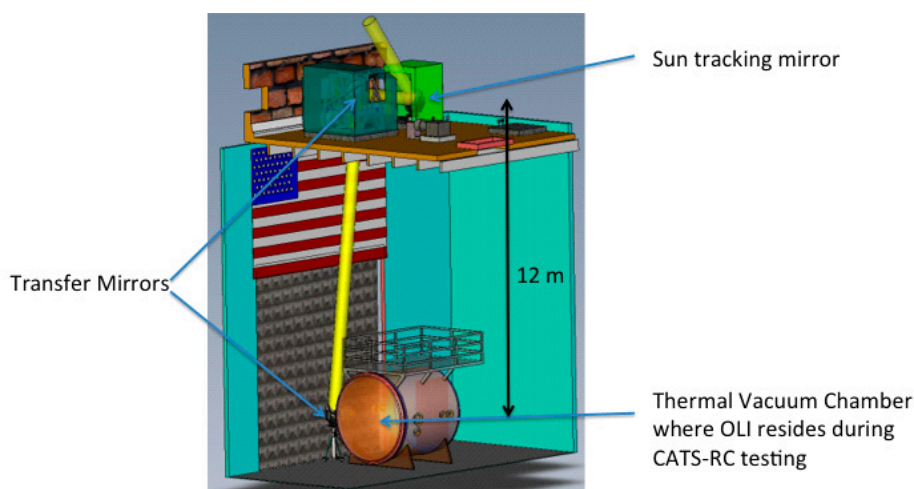
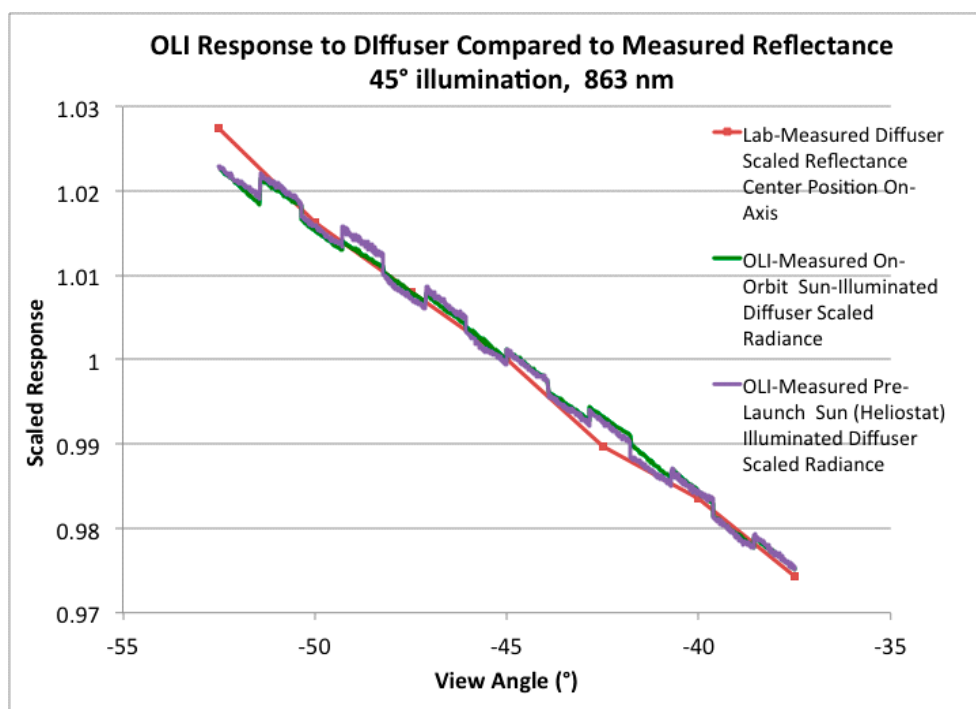


Figure 19. Comparison of Diffuser Reflectance to OLI Response to Diffuser.



In addition to the component level measurements of the diffuser reflectance factors, the installed OLI diffusers were illuminated by the sun (via a heliostat-Figure 18) and viewed by the OLI instrument, as

they would be on-orbit. The OLI was under thermal vacuum conditions for this testing. As a check on the uniformity of the heliostat and the diffuser and the cross track consistency of the OLI radiometric calibration, the shape of the OLI measured radiance (based on the DSS-based calibration) of the sunlight reflected off the diffuser panel is compared to the measured reflectance of the panel at the panel center position (Figure 19). Note that the odd and even FPMs view the diffuser panel on opposite sides of the principal plane of the sun and diffuser normal, leading to small discontinuities in response at the FPM boundaries. Also, as shown in Figure 15, each FPM views a somewhat different portion of the diffuser panel, which can also lead to some of the differences shown in the plots. Overall, note that the internal consistency of the measurements is within $\pm 0.5\%$ across the full field of view.

5. OLI Transfer to Orbit Experiment

The heliostat measurements described above were primarily acquired as part of a “transfer-to-orbit” experiment to assess the stability of the OLI instrument through the launch and early-on-orbit transition. The tenets behind this experiment were:

- (1) The OLI diffusers would be the most stable artifact through the launch and early-on-orbit period (as opposed to the lamps or the OLI itself)
- (2) The OLI response to the diffusers could be measured both prior to launch and on-orbit using the same illumination source (namely the sun).
- (3) The transmission losses in the atmosphere and heliostat could be sufficiently quantified for all but the cirrus band to allow the pre-launch test to be corrected to post launch conditions with an uncertainty of a few percent or less.

The ground portion of the testing occurred while the OLI was under thermal vacuum conditions in the CATS test set up. On two days with clear atmospheric conditions, the heliostat was activated, bringing sunlight from the roof into a side port of the thermal vacuum chamber (Figure 18). A solar radiometer tracked the sun and measured the atmospheric transmittance during the test. On each day the working and pristine diffusers were alternatingly deployed and OLI data were acquired while the clear sky conditions persisted. The heliostat transmittance was measured before and after this testing using a spectrometer that measured the beam radiance off of a diffuser before and after transiting the heliostat [23,24].

The on-orbit radiances of the diffuser ($\hat{L}_{\text{band,TOA}}$) were predicted as:

$$\hat{L}_{\text{band,TOA}} = L_{\text{band,helio}} / (T_{\text{band,helio}} \times T_{\text{band,atm}}) (D_{\text{E-S,helio}} / D_{\text{E-S,orbit}})^2 \quad (1)$$

where:

$L_{\text{band,helio}}$ is the OLI measured radiance of the diffuser illuminated via the heliostat using OLI’s DSS-based calibration

$T_{\text{band,helio}}$ is the measured transmittance of heliostat

$T_{\text{band,atm}}$ is the transmittance of the atmosphere at the time of the heliostat measurement.

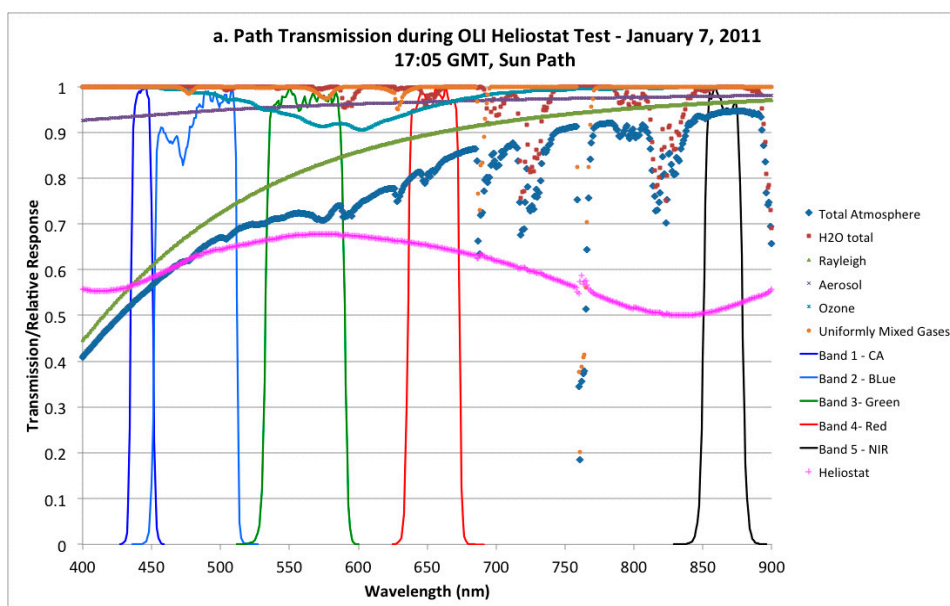
$D_{\text{E-S,helio}}$ is the Earth-Sun distance at the time of the heliostat observation

$D_{\text{E-S,orbit}}$ is the Earth-Sun distance at the time of the on-orbit observation.

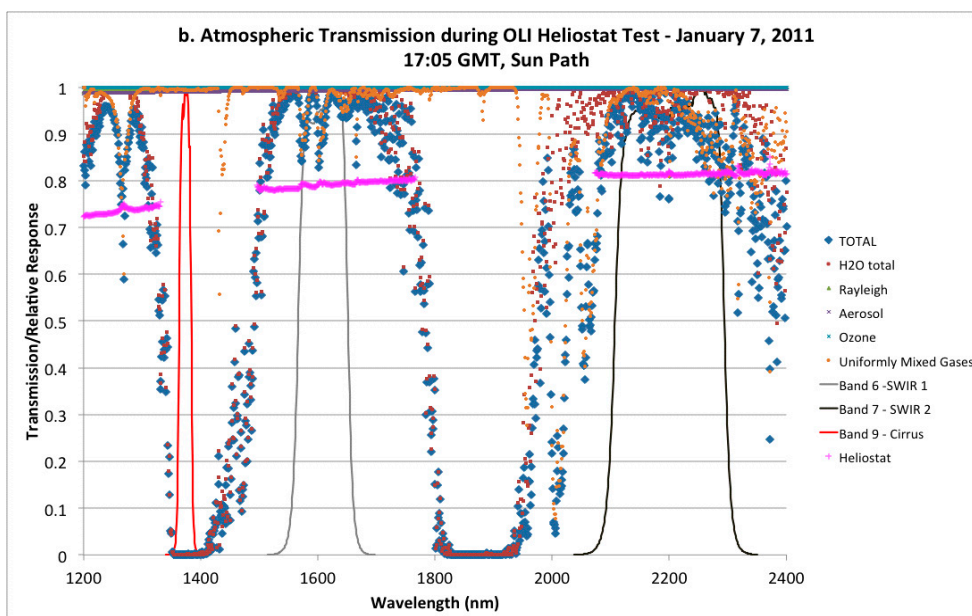
$T_{\text{band,atm}}$ was calculated using MODTRAN [25] based on the atmospheric pressure (T_{rayleigh}), the solar radiometer measurements (T_{aerosol}) and atmospheric gaseous abundances (T_{gases}).

Water vapor abundances were determined from the solar radiometer measurement and the ozone abundance came from OMI data [26]. Other gaseous abundances were based on values built into MODTRAN. The transmittances determined for one of the heliostat tests are shown in Figure 20 in relation to the OLI bandpasses.

Figure 20. Atmospheric and heliostat transmissions used to correct OLI transfer to orbit data to top of atmosphere values. (a) VNIR; (b) SWIR.



(a)



(b)

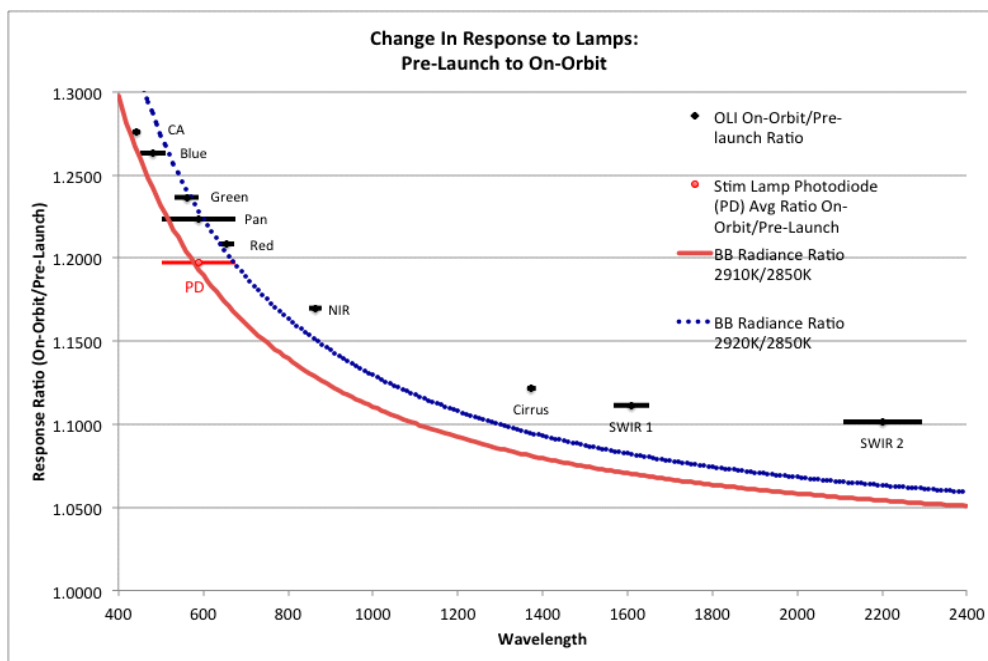
The estimated uncertainty in the heliostat transmittance, based on multiple measurements with different techniques was ~1.5% ($k = 1$); for the atmospheric transmittance ~2% ($k = 1$); for a total estimated uncertainty in transmittance of ~2.5% ($k = 1$). The OLI data were bias corrected by subtracting the nearest shutter collect values, linearized and converted to radiance using the pre-launch radiance

calibration coefficients. These radiances were converted to the predicted on-orbit radiances by dividing by the heliostat and atmospheric transmittances. Each collect on 7 January 2011, the better of the two days acquired was analyzed separately (four working collects and four pristine collects).

Once launched and after instrument activation, bench dry-out and cool down to operational temperatures, the on-orbit portion of the transfer to orbit experiment was completed. A working solar diffuser collect and a pristine solar diffuser collect were both performed on 18 March 2013 (mission day 35) and this was repeated on 28 March 2013 (mission day 45). These data were converted to radiance, L_{obs} , using the same procedure and coefficients as the pre-launch heliostat data. The results are shown in Table 2.

A second method for evaluating the stability of the OLI responsivity in the transition from on-Earth to in-orbit comes from the stim lamps and their built-in radiance monitor. The OLI stim lamps are tungsten halogen lamps and are operated in a constant current mode. It has been widely observed [27], that this type of lamp, operated in this manner, will burn significantly warmer and therefore brighter in a “zero gravity” state. The conventional wisdom is that this is due to the lack of convectional cooling of the filament in a zero gravity environment. In addition to the hotter temperature, the zero gravity environment would be expected to change the filament shape.

Figure 21. OLI and stim lamp photodiode monitor changes in response to stim lamps. Horizontal bars indicate the bandpasses. Blackbody temperature shifts matching the panchromatic band observed change (blue) and the photodiode observed change (red) are shown for reference.



As shown in Figure 21 the change in response of the OLI instrument to the stim lamps between pre-launch testing (CATS) and on-orbit measurements is a smooth function of wavelength, from about 28% increase in the shortest wavelength to about 10% increase at the longest wavelength. Also shown are the modeled differences expected if the change was strictly a color temperature increase of 60 or 70 K assuming no other emissivity or transmissivity changes in the lamp or lamp assembly. The OLI

changes do not match a blackbody temperature shift well. The photodiode response change to the stim lamp between the same observations was 2.5% less than the spectrally comparable OLI pan band. A 60 K color temperature (red line) increase that matched the photodiode response change in the panchromatic band, was used to calculate the response change in the spectrally overlapping red and green bands. These response changes are compared to the heliostat-based response changes in Figure 22 (using heliostat results from Table 2). The uncertainty in the photodiode-based response change is estimated at 1% based on its pre-launch stability viewing the stim lamp, though any launch-related shift is unknown.

Figure 22. Estimated OLI responsivity changes on transfer to orbit using heliostat test (from Table 2) and stim lamps with photodiode response.

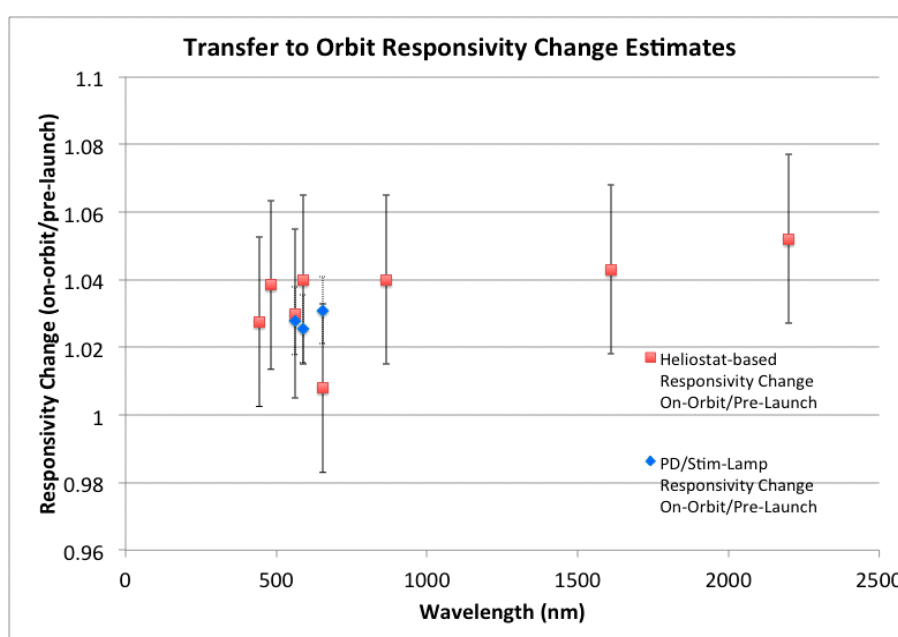


Table 2. Predicted OLI radiance of working diffuser based on heliostat test ($\hat{L}_{band, TOA}$) compared to observed radiance assuming unchanged instrument responsivity (L_{obs}), $L_{obs}/_{band, TOA}$.

	CA	Blue	Green	Red	NIR	SWIR 1	SWIR 2	Pan
Mean	1.033	1.040	1.029	1.007	1.038	1.045	1.051	1.041
StDev	0.009	0.007	0.005	0.006	0.005	0.004	0.005	0.005

6. OLI On-Orbit Reflectance Calibration

Using the same 18 March 2013 solar diffuser acquisition as used for the transfer to orbit experiment, the initial on-orbit reflectance calibration of the OLI was performed.

Theoretically, for detector d of a given band:

$$G_r[d] = (Q_{SDnetlin}[d] (D_{ES,SD})^2) / (BRF[d] \cos(\theta_{s,SD})) \tag{2}$$

where:

$G_r[d]$ is the reflectance Gain for detector d in DN/unit reflectance

$BRF[d]$ is the Bidirectional Reflectance Factor of the solar diffuser for the illumination and view angles for detector d

$\theta_{s,SD}$ is the solar incidence angle for this diffuser observation (always 45°)

$Q_{SDnetlin}[d]$ is the bias and non-linearity corrected response for detector d to the diffuser for this observation in DN

$D_{ES,SD}$ is the Earth-Sun distance for this diffuser observation in Astronomical Units

For this analysis we chose the center detector in FPM 7 for the tie to absolute reflectance calibration and used the relative gains of the OLI from pre-launch testing to propagate the absolute gain to the other detectors. The BRF values from the prelaunch measurements from location 3 on the panel were interpolated to the angles the panel is viewed by this detector. The reflectance gains are not stored explicitly in the calibration parameter file; the radiance to reflectance conversion factor, defined as the ratio of the radiance gain to the reflectance gain is stored as REFLECTANCE_CONVERSION factors, one value per band. The estimated uncertainty in the reflectance calibration using these factors is 2% ($k = 1$).

7. Calibration Updates

Several radiometric calibration updates were performed that affected the absolute calibration of OLI data. These went into effect on 3 February 2014 for both new data and older data, which were reprocessed. These changes were:

- (1) The cirrus band reflectance calibration was corrected for an error found in the calculation; this increased the reflectance in this band by $\sim 7\%$, without changing the radiance calibration.
- (2) The SWIR-2 band gain was adjusted for the difference observed prior to launch between the BATC and validation results; this increased the radiance by about 3%, without changing reflectance calibration.
- (3) All bands gains were adjusted to correct for an outdated radiance file that was mistakenly used in the pre-launch calibration data reduction for all bands; this decreased the radiance in all bands by $\sim 2\%$, without changing the reflectance calibration.
- (4) The precision of the radiance to reflectance conversion was improved for all bands; this was a less than 1% effect in reflectance.

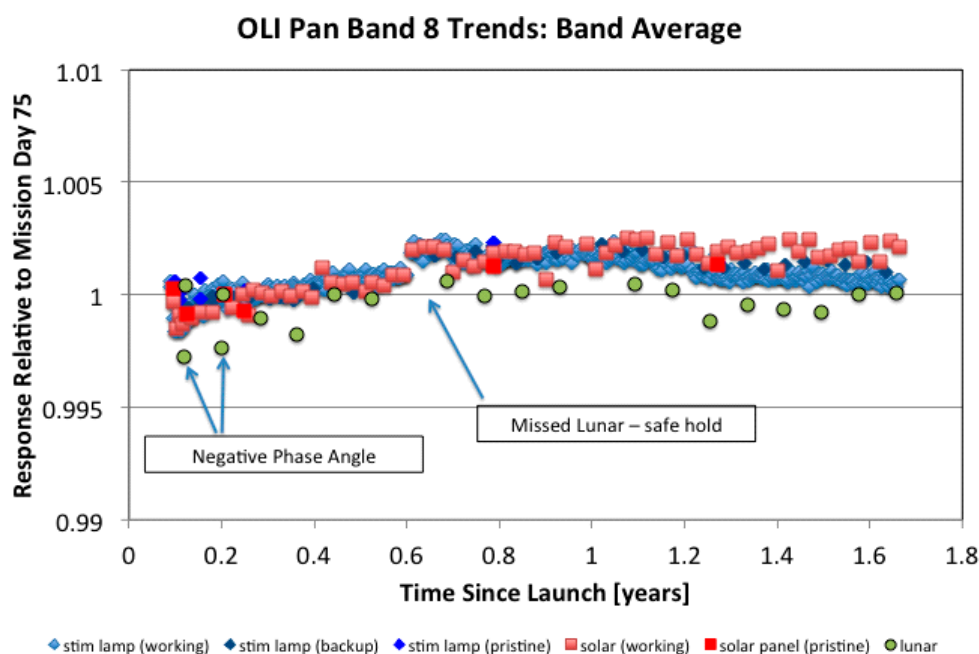
8. Stability over Mission

Once on-orbit, radiometric-calibration related acquisitions (lamp, solar, lunar) were performed per the schedules shown in Section 2. Data from each of these acquisitions were processed through the Image Assessment System (and, for lunar data, compared to the Lunar irradiance model) to obtain the band average responses or gains. These results are trended over time, after normalization to put them all on the same relative scale. The normalization was performed relative to the results from mission day 75, a day when there were collects from all calibrators acquired within ± 1 day.

An example band (pan band) (Figure 23) shows features common to all plots, *i.e.*,

- (1) Two of the early lunar acquisitions were at $\sim -7^\circ$ phase angle *versus* the $\sim +7^\circ$ phase angle for the remainder of the collects. These two negative phase angle points are outliers.
- (2) A safe hold event at about 0.6 years into the mission power cycled the OLI instrument. This resulted in small changes in the responsivity of bands 1–4 and 8 of 0.1 to 0.2%. This change in response recovered about 0.1 years later for reasons currently unknown.

Figure 23. OLI on-orbit radiometric calibration results across the current mission lifetime for the pan band.



General observations on the OLI stability (Figure 24) are:

- (1) The OLI average response is stable to within $<1\%$ over the first 1.6 years.
 - The CA band has the largest change, about 1.0%, and the change is consistent across all of the calibration techniques.
- (2) Different calibration sources generally agree to within a few tenths of a percent in the trends.
 - Several bands show a 0.1% to 0.3% increase in response apparent in the lamp and solar data, but less so in the lunar data.
 - The origin of lower precision of the lunar results, particularly in the SWIR bands, is currently under study and may be related to the integration technique.
- (3) The divergence in the lamp and working diffuser results may indicate that the working diffuser is brightening, particularly in the NIR and SWIR.

Additional information about the stability of the OLI and the OLI stim lamps can be obtained from the OLI telemetry. Trends for several temperatures as well as the lamp currents, voltages and photodiode responses are shown in Figure 25.

Figure 24. OLI on-orbit radiometric calibration results across the current mission lifetime for each band.

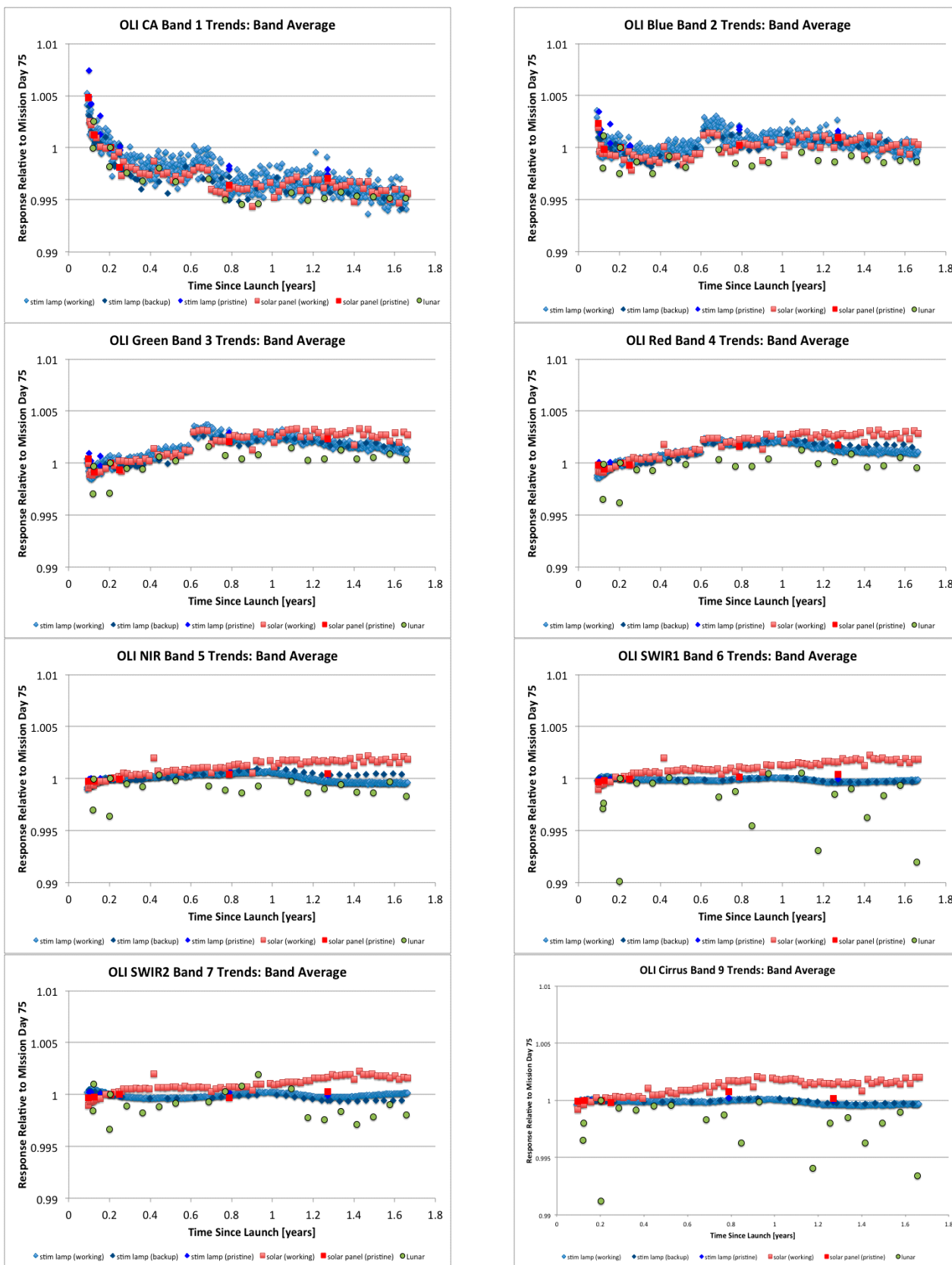
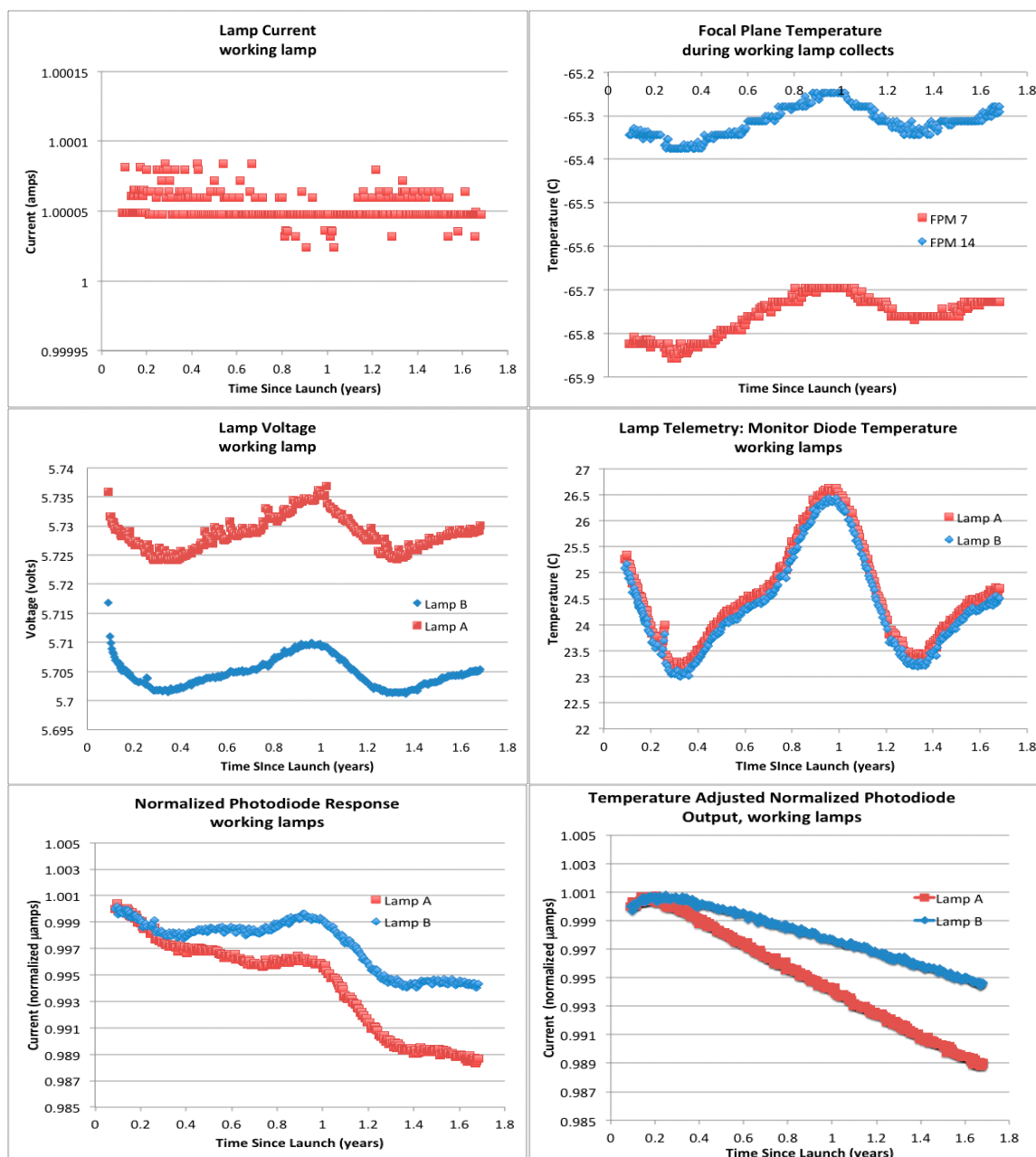


Figure 25. OLI Telemetry Mission Trends.



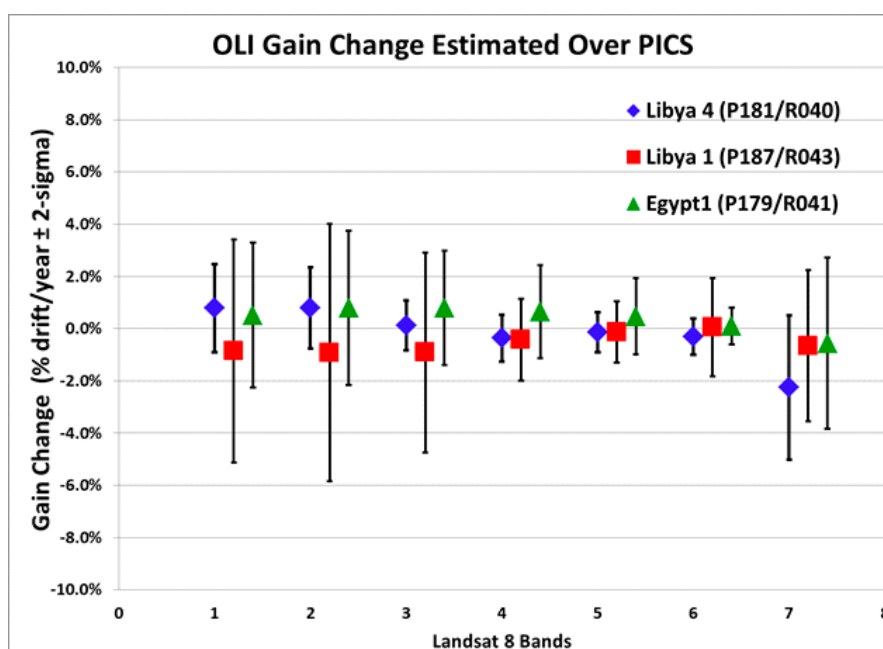
Several observations on the telemetry:

- (1) The telemetry indicates that constant current is maintained through the stim lamps at the better than $\pm 0.01\%$ level.
- (2) The OLI focal plane has been maintained to better than ± 0.1 °C across the mission; some seasonal variation is evident.
- (3) The lamp voltage varies by about $\pm 0.1\%$ across the mission according to the telemetry and shows a correlation to the instrument temperature.
- (4) The photodiode monitors show an apparent decrease in the stim lamp radiance of $\sim 0.5\%$ over the mission lifetime and there is apparent temperature sensitivity in the trend. Adjusting for the temperature sensitivity (Figure 14d) removes most of the structure, but leaves a nearly linear degradation with time. The spectrally comparable OLI

panchromatic band (band 8) shows a flat to slightly increasing response to the working stim lamps, which closely matches the response to the diffusers, suggesting the change is in the monitoring circuit.

The OLI stability is also monitored relative to Pseudo-Invariant Calibration Sites (PICS) [28], desert sites in North Africa that have been selected for their stability. The same area on the ground is selected for each acquisition over these sites, averaged and adjusted for the solar zenith angle and Earth-Sun distance. The adjusted responses are regressed over time to determine any temporal drift. Figure 26 shows the estimated drift or gain change of each of the OLI bands relative to these sites. Other than cloud screening, there is no adjustment for site or atmospheric variation with time, so these determine the within and between site variability. Note that no changes are evident within the uncertainty of the technique.

Figure 26. OLI stability relative to desert calibration sites.

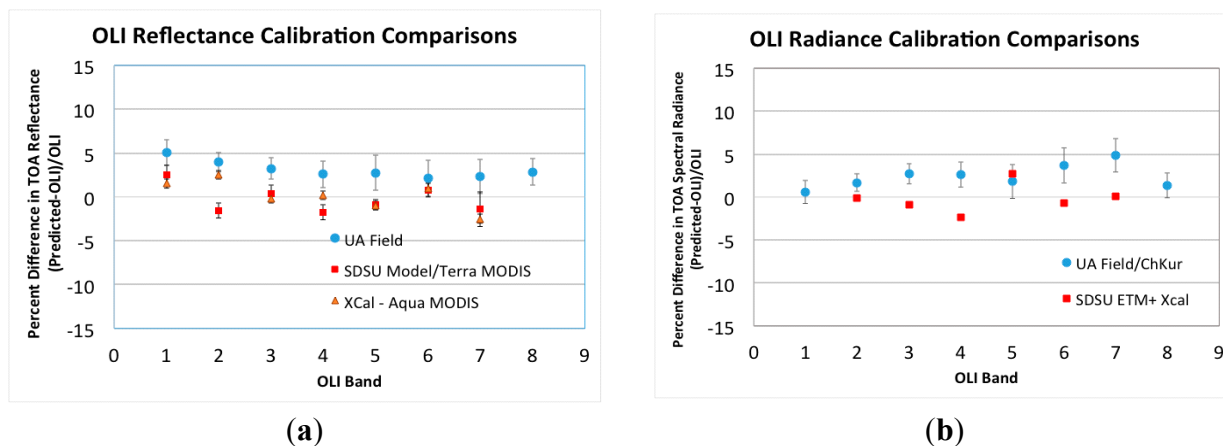


9. Comparison to Other Measurements

A number of comparisons have been performed between the OLI data and ground measurements (usually referred to as vicarious calibration) and other on-orbit sensors (usually called cross calibration) and are discussed in detail in other papers in this special issue [2,3].

A summary of the early on-orbit comparisons to the reflectance-based calibration of OLI, shown in Figure 27a, generally show agreement to within the uncertainty in the OLI reflectance calibration (2%, $k = 1$) and the reference techniques (note that the error bars shown are precision, not total uncertainty which is in on the order of 3% for the best of the vicarious techniques). The University of Arizona vicarious measurements have a bias relative to the OLI reflectance calibration (with OLI being low) averaging about 3%. The difference is the largest in the CA band, where the other methods suggest a negative bias as well, though smaller.

Figure 27. Comparisons of OLI operational radiometric calibrations to other measurements [2,3]: (a) Reflectance calibration; (b) Radiance calibration.



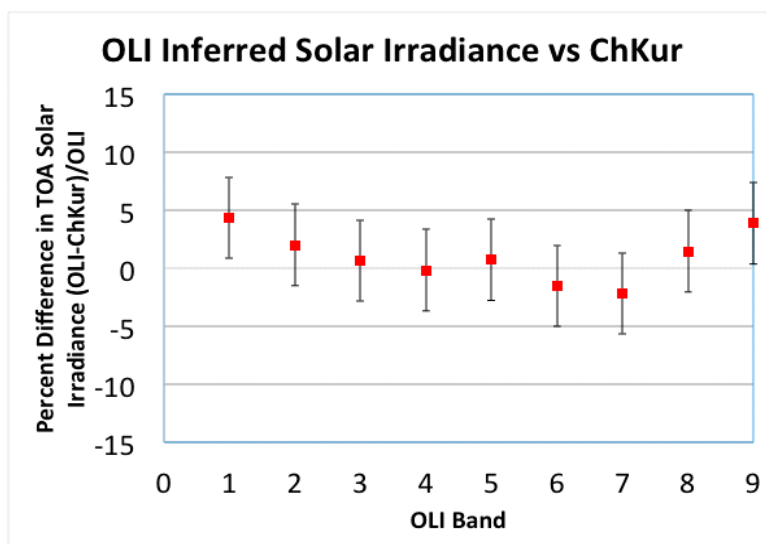
In the radiance domain, the results are similarly consistent, where the OLI radiance uncertainty is about 3% (Figure 27b). Note that the radiance UA results, which use the same data as the UA reflectance calibrations, but converted to radiance with a solar model, point out an inconsistency of the OLI calibrations with the solar model (Chkur) at the shortest wavelength of about 4%. In other words, given that OLI has independent reflectance and radiance calibrations, a solar irradiance can be determined from OLI diffuser observations. This OLI inferred solar irradiance ($ESUN_{OLI}$) can be calculated from the REFLECTANCE_CONVERSION factors as:

$$ESUN_{OLI}(b) = \pi / REFLECTANCE_CONVERSION(b) \tag{3}$$

where b is the OLI band.

The uncertainty in the OLI based solar irradiances is about ~3.5%, given the ~2% reflectance uncertainty and ~3% radiance uncertainty. As shown in Figure 28, the $ESUN_{OLI}$ to $ESUN_{CHKUR}$ are within 2% of the each other, except in the Coastal Aerosol and Cirrus bands. The difference in the CA and Cirrus bands may be significant.

Figure 28. OLI inferred solar irradiance as compared to ChKur solar irradiance. Estimated uncertainty in OLI derived solar irradiance is shown.



10. Discussion

The OLI's radiometric stability and absolute radiometric calibration performance are excellent. Firstly, the instrument has been very stable on-orbit, with little to no degradation during the early on-orbit period, where changes typically occur. Over the first 1.6 years of operation, only the CA band shows a measurable degradation of approximately 1.0% and the results are consistent between calibration techniques at about the 0.1% level. Other bands show changes at the 0.1% to 0.2%, but are not consistent across all methods. This type of performance and consistency between on-board calibration techniques is unprecedented in Landsat instrument history and rare in Earth imaging systems in general. Landsat-7 ETM+, for example, had three on-board calibration devices and none of these three was as stable as the instrument itself. By the same point in the mission history, the calibration devices showed changes as much as 5% in the opposite directions [29]. And although the instrument itself appeared to be almost as stable as OLI (it did not have a coastal aerosol band), it took many years using vicarious calibration techniques to demonstrate this, and the ultimate confidence in this stability is much lower than OLI. Solid design, component selection and screening, contamination control and pre-launch characterization all contributed to this success. Secondly, the comparisons to ground measurements and other on-orbit assets generally show OLI absolute radiance and reflectance calibrated operational products consistent within the uncertainties of the techniques and the uncertainties in the OLI calibrations (2% to 3%). The combination of the radiance and reflectance calibrations can produce within band solar spectral irradiances at uncertainties approaching the current standards.

Two aspects of the OLI and/or the OLI calibration devices are not well understood. Firstly, the stim lamp photodiode shows changes in response to the stim lamps that do not track to within better than 2% of the spectrally comparable OLI band. This occurs in the pre-launch realm; the transfer to orbit, where the photodiode reports smaller changes in the stim lamps than the OLI; and in the on-orbit periods, where the photodiode shows about a 1% drop in lamp output that is not apparent in the OLI response. The post-launch change in the photodiode monitor response to the stim lamp appears likely to be due to something in the monitor or its circuitry, as the OLI response to the stim lamps shows little difference from the OLI response to the diffusers over time.

Secondly, the heliostat based transfer to orbit experiment indicates increased responsivity (3%–5%) in many of the OLI bands at a level greater than the estimated uncertainty in the technique (2.5%). Additionally, as noted above, the stim lamp photodiode reports a smaller increase in lamp radiance than the OLI on orbit, which is consistent with the heliostat transfer to orbit experiment. In general, if the corresponding OLI band responsivity increase is incorporated, the agreement of the radiance calibrations to ground measurements or other satellites does not improve.

11. Conclusions

The OLI instrument on Landsat-8 was extensively characterized prior to launch and radiometrically calibrated prior to launch and on-orbit. Once on orbit, the OLI instrument has been extremely stable, changing by than less than 1% in responsivity over the first year plus of operations. The OLI data are calibrated both in radiance units and reflectance units as part of the data processing and the users are provided coefficients to convert to either unit. Error analyses indicate that the reflectance product has a

lower uncertainty (~2%), and it is generally has been recommended that users work with the reflectance calibration because of this. However, both products appear to be within their uncertainty requirements.

Comparisons to other sensors have given mixed answers as to whether the OLI reflectance or radiance calibration is more accurate. Also, the OLI reflectance and radiance calibration are currently independent, *i.e.*, not tied to a specific solar irradiance model. The question arises as to whether that by accepting one of the OLI calibrations as “correct”, *e.g.*, the reflectance calibration, and converting to radiance with an accepted solar irradiance dataset, provides a better radiance calibration (or *vice versa*).

This research has demonstrated that the OLI instrument is the best radiometrically calibrated reflective Landsat sensor to date. Work is now in progress to tie the full Landsat record to the OLI instrument, to provide a consistent data archive for assessing land cover and land use change.

Acknowledgments

Building and calibrating a flight instrument involves a large team of people with various skills. None of this work could have been accomplished without that team effort and it would take a lot of space to identify all of those involved. We would particularly like to identify several organizations and individuals, which although not identified as authors, were large contributors.

Goddard LDCM project management, particularly Jeanine Murphy-Morris, the OLI Instrument Manager, for her accommodations and support for these efforts.

BATC systems engineering team, including Ed Knight, Brent Canova, Eric Donley, Brian Donley, Amy Newbury, Roger Drake, Sandra Collins, Khurram Ansari, and Leanne Presley.

BATC Integration and Test Team, including Warren Lotz, Jeff Parker and many others.

Linda Fulton, BATC calibration systems lead and lead test director.

Hansford Cutlip, Ground Calibration Test Equipment Lead.

Jeffrey Pedelty, NASA on-site representative at BATC and ex-officio Cal Team Member.

Jim Storey, Ron Morfitt, Ron Hayes, USGS/EROS Calibration Team Leads.

Tom Stone, USGS Lunar Irradiance Model Lead.

Phil Dabney, NASA instrument scientist and ex-officio Cal Team Member.

Carol Johnson and Stephen Maxwell, NIST collaborators.

Funding identification:

Ball Aerospace’s work and the University of Arizona’s BRDF characterizations were performed under NASA Contract NNG07HW18C.

Science Systems and Applications work was performed under NASA contract NNG09HP18C.

South Dakota State University analyses were performed under NASA cooperative agreement NNX09AH23A.

Author Contributions

Several authors contributed to most sections of this paper, including Brian Markham, Julia Barsi and Geir Kvaran. Geir was the lead system engineer at BATC for the radiometric calibration of the OLI during the pre-launch and commissioning phases; as such he had primary responsibility for planning the tests and analyzing the data. Lawrence Ong’s contributions covered multiple areas, but the lunar

calibration (Section 2.3) and the radiometer comparison campaign (Section 3.1) were his major contribution. Ed Kaita was involved in much of the data analysis, particularly the diffuser characterization, transfer to orbit experiment and on-orbit diffuser analyses (Sections 4, 5 and 8). Stuart Biggar characterized the OLI flight diffusers in the University of Arizona lab (Section 4) and measured the OLI calibration sources with radiometers (Section 3.1). Jeff Czapla-Myers performed the atmospheric characterization as part of the transfer to orbit experiment (Section 5) and performed extensive field measurements during the commissioning phase (Section 9). Nischal Mishra and Dennis Helder performed cross calibrations and evaluated OLI stability relative to the PICS sites (Section 8).

Conflicts of Interest

The authors declare no conflict of interest.

References

1. Knight, E.J.; Kvaran, G. Landsat-8 Operational Land Imager design, characterization, and performance. *Remote Sens.* **2014**, *6*, 10286–10305.
2. Czapla-Myers, J.; McCorkel, J.T.; Anderson, N.; Thome, K.J.; Bigger, S.; Helder, D.L.; Aaron, D.; Leigh, L.; Mishra, N. The ground-based absolute radiometric calibration of Landsat 8 OLI. *Remote Sens.* **2014**, in press.
3. Mishra, N.; Haque, M.O.; Leigh, L.; Aaron, D.; Helder, D.L.; Markham, B.L. Radiometric cross calibration of Landsat 8 Operational Land Imager (OLI) & Landsat 7 Enhanced Thematic Mapper Plus (ETM+). *Remote Sens.* **2014**, in press.
4. Kvaran, G.; Markham, B.; Zalewski, E. Overview of the radiometric calibration of the Operational Land Imager (OLI). In Proceedings of the 19th Annual Conference on Characterization and Radiometric Calibration for Remote Sensing (CalCon), Logan, UT, USA, 23–26 August 2010.
5. Tsai, B.; Allen, D.; Cooksey, C.; Yoon, H.; Fulton, L.; Kvaran, G.; Biggar, S.; Markham, B. Calibration of Landsat/OLI panels using the NIST BRDF scale from 1100 to 2400 nm. In Proceedings of the 19th Annual Conference on Characterization and Radiometric Calibration for Remote Sensing (CalCon), Logan, UT, USA, 23–26 August 2010.
6. Cutlip, H.; Chase, H.; Fulton, L.; Schneider, L.; Pierce, A.; Gleeson, D.; Kvaran, G.; Canova, B.; Johnson, C.; Saunders, R.; *et al.* OLI radiometric calibration: Ground support equipment characterization and calibration. In Proceedings of the 19th Annual Conference on Characterization and Radiometric Calibration for Remote Sensing (CalCon), Logan, UT, USA, 23–26 August 2010.
7. Collins, S.; Good, W.; Cutlip, H.; Seerveld, J.; Kaptchen, P.; Kvaran, G. Operational Land Imager: Using the Sun as the source for ground based radiometric calibration. In Proceedings of the 19th Annual Conference on Characterization and Radiometric Calibration for Remote Sensing (CalCon), Logan, UT, USA, 23–26 August 2010.
8. Kvaran, G.; Markham, B.; Leisso, N.; Czapla-Myers, J.; Biggar, S. OLI radiometric calibration. In Proceedings of the 20th Conference on Characterization and Radiometric Calibration for Remote Sensing (CalCon), Logan, UT, USA, 29 August–1 September 2011.

9. Biggar, S.; Anderson, N.; Fulton, L.; Kvaran, G.; Kortmeyer, H. Reflectance factor measurements of the OLI flight diffusers. In Proceedings of the 20th Conference on Characterization and Radiometric Calibration for Remote Sensing (CalCon), Logan, UT, USA, 29 August–1 September 2011.
10. Cutlip, H.; Cole, J.; Johnson, B.C.; Maxwell, S.; Markham, B.; Ong, L.; Hom, M.; Biggar, S. The OLI radiometric scale realization round robin measurement campaign. In Proceedings of the 20th Conference on Characterization and Radiometric Calibration for Remote Sensing (CalCon), Logan, UT, USA, 29 August–1 September 2011.
11. Kvaran, G.; Knight, E.; Ansari, K.; Lee, K.; Canova, B.; Donley, B.; Kieffer, H. Landsat-8 Operational Land Imager (OLI) initial on-orbit performance. In Proceedings of the 22th Conference on Characterization and Radiometric Calibration for Remote Sensing (CalCon), Logan, UT, USA, 19–22 August 2013.
12. Vanderwerff, K.; Morfitt, R. Bias estimation for the Landsat 8 Operational Land Imager. *Proc. SPIE* **2011**, 8153, doi:10.1117/12.896221.
13. Morfitt, R.; Markham, B.L.; Micijevic, E.; Scaramuzza, P.; Barsi, J.A.; Levy, R.; Ong, L.; Vanderwerff, K. OLI radiometric performance on-orbit. *Remote Sens.* **2014**, in press.
14. Eplee, R.; Barnes, R.; Patt, F.; Meister, G.; McClain, C. SeaWiFS lunar calibration methodology after six years on orbit. *Proc. SPIE* **2004**, doi:10.1117/12.556408.
15. Sun, J.; Xiong, X.; Barnes, W.; Guenther, B. MODIS reflective band on-orbit lunar calibration. *IEEE Trans. Geosci. Remote Sens.* **2007**, 7, 2383–2393.
16. Mendenhall, J.; Lencioni, D.; Evans, J.B. Spectral and radiometric calibration of the advanced land imager. *Linc. Lab. J.* **2005**, 15, 207–224.
17. Lacherade, S.; Aznay, O.; Fougny, B. POLO Pleiades Orbital Lunar Observations: Intensive study of the Moon and comparison to ROLO model. In Proceedings of the 22th Conference on Characterization and Radiometric Calibration for Remote Sensing (CalCon), Logan, UT, USA, 19–22 August 2013.
18. Kieffer, H.H.; Stone, T.C. The spectral irradiance of the Moon. *Astron. J.* **2005**, 129, 2887–2901.
19. University of Arizona, College of Optical Sciences, Remote Sensing Group, Transfer Radiometers. Available online: <http://fp.optics.arizona.edu/RSG/resources.php?content=transfer> (accessed on 15 May 2014).
20. Butler, J.; Barnes, R. The use of transfer radiometers in validating the visible to shortwave infrared calibrations of radiance sources used by instruments in NASA's Earth Observing System. *Metrologia* **2003**, 40, S70–S77.
21. Brown, S.W.; Eppledauer, G.P.; Lykke, K.R. Facility for Spectral Irradiance and Radiance Responsivity Calibrations using Uniform Sources (SIRCUS). *Appl. Opt.* **2006**, 45, 8218–8237.
22. Landsat-8 Calibration Parameter Files (CPF) and Bias Parameter Files (BPF). Available online: <http://landsat.usgs.gov/cpfbpf.php> (accessed 1 June 2014).
23. Kuester, M.A.; Czaplá-Myers, J.; Kaptchen, P.; Good, W.; Lin, T.; Biggar, S.; Thome, K. Development of a heliostat facility for solar-radiation-based calibration of Earth observing sensors. *Proc. SPIE* **2008**, doi:10.1117/12.794228.

24. Czapla-Myers, J.; Thome, K.; Anderson, N.; McCorkel, J.; Leisso, N.; Good, W.; Collins, S. Transmittance measurement of a heliostat facility used in the preflight radiometric calibration of Earth-observing sensors. *Proc. SPIE* **2009**, doi:10.1117/12.828873.
25. Berk, A.; Anderson, G.; Acharya, P.; Shettle, E. *MODTRAN 5.2.0.0. User's Manual*; Air Force Geophysical Laboratory: Hanscom AFB, MA, USA, 2008; p. 100.
26. Space Based Measurements of Ozone and Air Quality in the Ultraviolet and Visible. Available online: http://ozoneaq.gsfc.nasa.gov/ozone_overhead_all_v8.md (accessed on 1 May 2014).
27. Butler, J.J., Johnson, B.C., Barnes, R.A. The calibration and characterization of Earth remote sensing and environmental monitoring instruments. In *Optical Radiometry*; Parr, A.C., Datla, R.U., Gardner, J.L., Eds.; Elsevier Academic Press: New York, NY, USA, 2005; pp. 488–494.
28. Cosnefroy, H.; Leroy, M.; Briottet, X. Selection and characterization of Saharan and Arabian desert sites for the calibration of optical satellite sensors. *Remote Sens. Environ.* **1996**, *58*, 101–114.
29. Markham, B.L.; Thome, K.J.; Barsi, J.A.; Kaita, E.; Helder, D.L.; Barker, J.L.; Scaramuzza, P.L. Landsat-7 ETM+ on-orbit reflective-band radiometric stability and absolute calibration. *IEEE Trans. Geosci. Remote Sens.* **2004**, *42*, 2810–2820.

© 2014 by the authors; licensee MDPI, Basel, Switzerland. This article is an open access article distributed under the terms and conditions of the Creative Commons Attribution license (<http://creativecommons.org/licenses/by/4.0/>).